#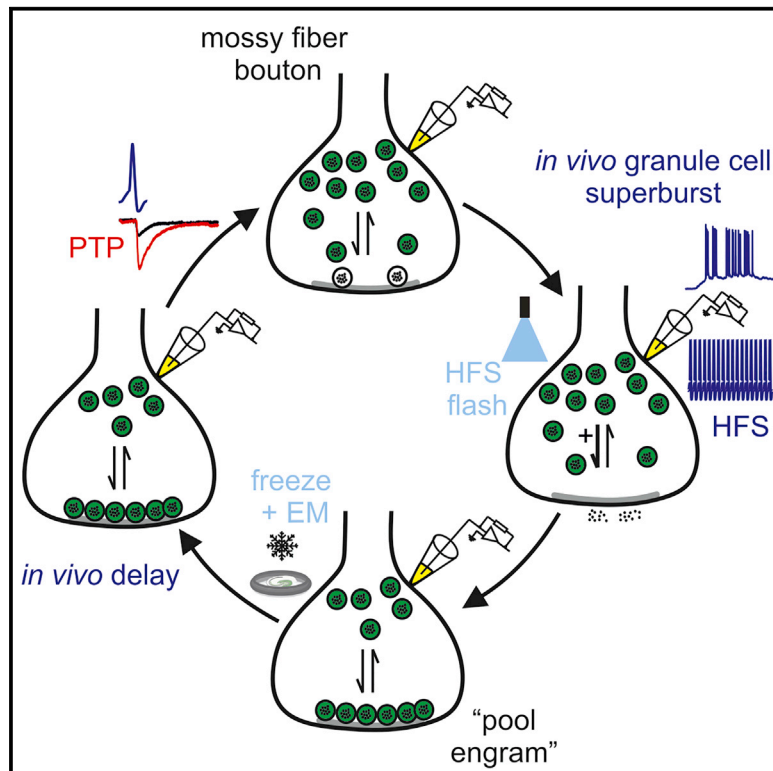 Short-Term Plasticity at Hippocampal Mossy Fiber Synapses Is Induced by Natural Activity Patterns and Associated with Vesicle Pool Engram Formation

Graphical Abstract

Authors

David Vandael,
Carolina Borges-Merjane,
Xiaomin Zhang, Peter Jonas

Correspondence

peter.jonas@ist.ac.at

In Brief

Vandael et al. report that natural activity patterns induce post-tetanic potentiation (PTP) at hippocampal mossy fiber synapses. PTP is primarily caused by an increase in the readily releasable vesicle pool. PTP is associated with an increase in the docked vesicle pool, revealing a structural correlate of presynaptic plasticity.

Highlights

- Natural activity patterns in hippocampal GCs *in vivo* induce PTP at mossy fiber synapses

- PTP is primarily caused by an increase in the readily releasable vesicle pool

- PTP is associated with an increase in the number of docked vesicles at active zones

- Sparse activity extends pool engram lifetime, increasing overlap with short-term memory

CellPress

Article

Short-Term Plasticity at Hippocampal Mossy Fiber Synapses Is Induced by Natural Activity Patterns and Associated with Vesicle Pool Engram Formation

David Vandael,[1] Carolina Borges-Merjane,[1] Xiaomin Zhang,[1] and Peter Jonas[1,2,*]
[1]Cellular Neuroscience, Institute of Science and Technology (IST) Austria, Am Campus 1, 3400 Klosterneuburg, Austria
[2]Lead Contact
*Correspondence: peter.jonas@ist.ac.at
https://doi.org/10.1016/j.neuron.2020.05.013

SUMMARY

Post-tetanic potentiation (PTP) is an attractive candidate mechanism for hippocampus-dependent short-term memory. Although PTP has a uniquely large magnitude at hippocampal mossy fiber-CA3 pyramidal neuron synapses, it is unclear whether it can be induced by natural activity and whether its lifetime is sufficient to support short-term memory. We combined *in vivo* recordings from granule cells (GCs), *in vitro* paired recordings from mossy fiber terminals and postsynaptic CA3 neurons, and "flash and freeze" electron microscopy. PTP was induced at single synapses and showed a low induction threshold adapted to sparse GC activity *in vivo*. PTP was mainly generated by enlargement of the readily releasable pool of synaptic vesicles, allowing multiplicative interaction with other plasticity forms. PTP was associated with an increase in the docked vesicle pool, suggesting formation of structural "pool engrams." Absence of presynaptic activity extended the lifetime of the potentiation, enabling prolonged information storage in the hippocampal network.

INTRODUCTION

Short-term memory, a form of memory that covers a timescale of tens of seconds to minutes, is an essential component of several brain functions, from the level of simple reflexes to the level of consciousness and intelligent behavior (Squire and Zola-Morgan, 1991; Goldman-Rakic, 1995). Early work suggested that sustained neuronal activity underlies short-term memory (Goldman-Rakic, 1995). However, more recent studies proposed that short-term memory is held in synapses, suggesting synaptic facilitation as a possible mechanism (Mongillo et al., 2008; Zenke et al., 2015; Jackman and Regehr, 2017). Although the idea that synaptic facilitation underlies short-term memory is appealing, the time course of facilitation is fast, decaying within tens to hundreds of milliseconds, whereas short-term memory extends over a much longer timescale. In the hippocampus, a brain region that contributes to short-term memory, information can be held in the circuit for several minutes during delayed match- or nonmatch-to-sample tasks (Squire and Zola-Morgan, 1991; Deadwyler et al., 1996). Thus, other forms of synaptic plasticity must be involved. A possible candidate might be post-tetanic potentiation (PTP), a form of short-term plasticity that decays within tens to hundreds of seconds (Zucker and Regehr, 2002). Within the hippocampus, PTP shows a unique magnitude at the mossy fiber-CA3 pyramidal neuron synapse, where PTP regulates synaptic strength by nearly an order of magnitude (Griffith, 1990; Langdon et al., 1995; Salin et al., 1996; Toth et al., 2000; Vyleta et al., 2016; reviewed by Nicoll and Schmitz, 2005). However, the physiological significance and

the biophysical mechanisms of mossy fiber PTP are largely unknown. Although previous attempts were made to test whether physiological activity patterns induce mossy fiber plasticity (Gundlfinger et al., 2010; Mistry et al., 2011), the results remained inconclusive, because the applied patterns were likely recorded from non-granule cells (Neunuebel and Knierim, 2012). Thus, whether mossy fiber PTP forms the basis of short-term memory in the hippocampus remains unclear.

To address the functional significance, mechanisms, and possible structural correlates of PTP at hippocampal mossy fiber synapses, we combined *in vivo* recordings from hippocampal granule cells (GCs) in behaving animals, *in vitro* paired recordings from mossy fiber terminals and postsynaptic CA3 pyramidal neurons (Vyleta et al., 2016), and functional electron microscopy (EM) analysis of mossy fiber synapses ("flash and freeze"; Watanabe et al., 2013a, 2013b; Borges-Merjane et al., 2020). Our results indicate that PTP is induced by physiological GC activity, generated by an increase in the size of the readily releasable vesicle pool (RRP), and associated with formation of structural "pool engrams."

RESULTS

Superbursts in GCs Induce PTP at Hippocampal Mossy Fiber-CA3 Synapses

To address whether hippocampal mossy fiber PTP is induced by natural activity patterns, we examined the activity of presynaptic dentate gyrus GCs in head-fixed behaving rodents (X.Z.,
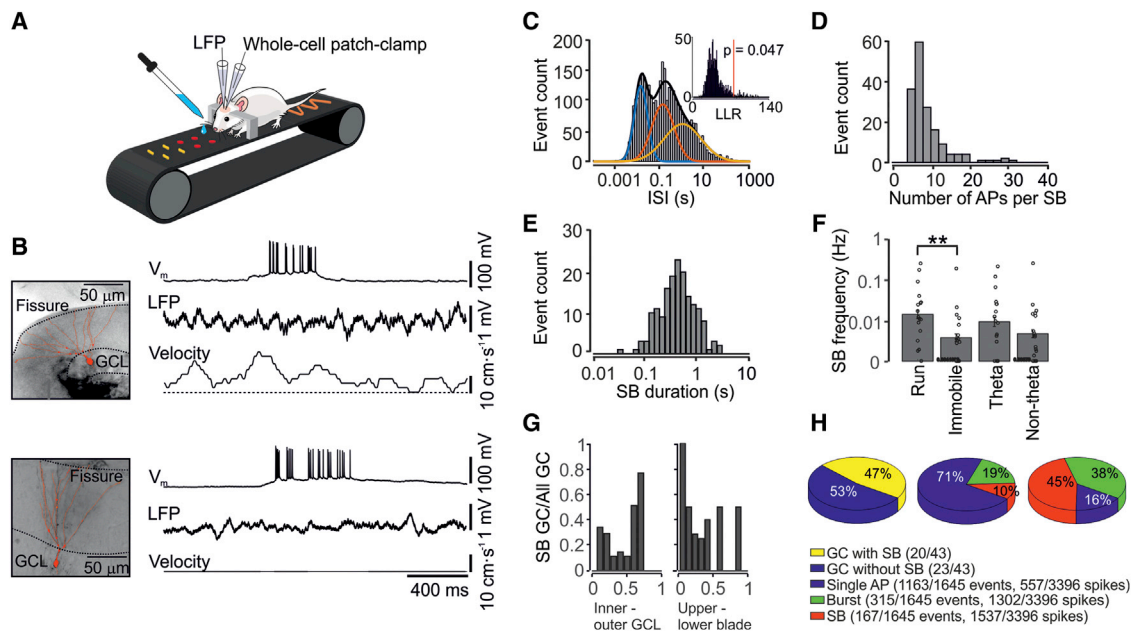
Figure 1. SB Activity in GCs in Awake Behaving Mice during Spatial Navigation

(A) Schematic illustration of the *in vivo* recording configuration. Mice were running on a linear belt. The belt surface had three partitions with different textures, providing tactile cues for spatial orientation.

(B) Left: light micrographs of two recorded neurons, superimposed with reconstruction. Somatodendritic morphology unequivocally identified the recorded neurons as dentate gyrus GCs. Dotted lines represent GC layer (GCL) boundaries and the hippocampal fissure, respectively. Right: current-clamp recording from the two GCs shown on the left. Top trace: intracellular membrane potential. Center trace: extracellular LFP. Bottom trace: velocity of the animal. The recorded GCs generated SBs with 18 and 26 APs, respectively.

(C) Histogram of ISIs. The black line represents fit with the sum of three log-normal distributions; colored lines indicate individual components. Inset: histogram of log-likelihood ratios (LLRs) for fits with three and two Gaussian functions from 1,000 bootstrap replications. The vertical red line indicates the measured LLR.

(D) Histogram of the number of APs per SB.

(E) Histogram of SB duration.

(F) Summary bar graph of SB frequency during running versus immobile periods and during theta versus non-theta periods. SB frequency is significantly higher during running periods. **$p < 0.01$. Boxes indicate mean values, and error bars denote SEM.

(G) Proportion of GCs showing SBs plotted against cell body location along the axis from the inner to the outer GC layer (left) and the axis from the upper to the lower blade (right). Note that GCs with SBs were observed in all parts of the dentate gyrus.

(H) Left: summary pie chart of the proportion of GCs that generated SBs. The total sample was comprised of 43 active GCs that generated APs during the recording period (5–30 min). Center: summary pie chart of the proportion of events (blue, single APs; green, bursts; red, SBs) in the total GC population. Right: summary pie chart of the proportion of APs (blue, APs occurring in isolation; green, APs contained in bursts; red, APs contained in SBs) in the total GC population. Note that the majority of spikes are contained in SBs.

A. Schlögl, and P.J., unpublished data; Figure 1). Simultaneous whole-cell current-clamp and local field potential (LFP) recordings were performed from GCs in the dorsal hippocampus during quiet and running periods (Figure 1A). Analysis of a total population of 43 morphologically identified active GCs revealed that, on average, GCs fired at low frequency (average firing frequency, 0.029 ± 0.011 Hz; mean ± SEM; X.Z., A. Schlögl, and P.J., unpublished data), consistent with previous immediate-early gene expression and Ca^{2+} imaging studies (Alme et al., 2010; Pilz et al., 2016). However, interspike intervals (ISIs) were widely distributed, indicating that activity was highly patterned (Figures 1B and 1C). ISI distributions were significantly better fit with the sum of three rather than two log-normal components, suggesting that activity was comprised of single spikes, bursts, and bursts of bursts ("superbursts" [SBs]) (p = 0.047; Figure 1C). On average, SBs contained 9.2 ± 0.5 spikes (Figure 1D) and had a mean duration of 603 ± 41 ms (Figure 1E). SBs were signif-

icantly more frequent during running than quiet periods (velocity >2 cm s^{-1}, 0.0197 ± 0.0086 Hz versus 0.0073 ± 0.0053 Hz, p = 0.004; Figure 1F). However, the SB frequency was not significantly different between theta and non-theta epochs (theta-to-delta power ratio in the LFP signal >4, 0.0149 ± 0.0069 Hz versus 0.0101 ± 0.0071 Hz, p = 0.309; Figure 1F). Thus, differences in SB frequency may be explained by direct effects of running rather than indirect effects of increased theta activity. The occurrence of SBs was independent of the location of the GC soma (Figure 1G). SBs occurred in 20 of 43 active GCs (Figure 1H, left). Event-based analysis showed that the majority of events (70.7%) were single spikes, whereas 19.1% were bursts, and 10.1% were SBs (Figure 1H, center). However, spike-based analysis revealed that only 16.4% of spikes occurred in isolation, whereas 38.3% and 45.3% occurred in bursts and SBs, respectively (Figure 1H, right). Thus, our results identify SBs as a prominent form of activity in the dentate gyrus.
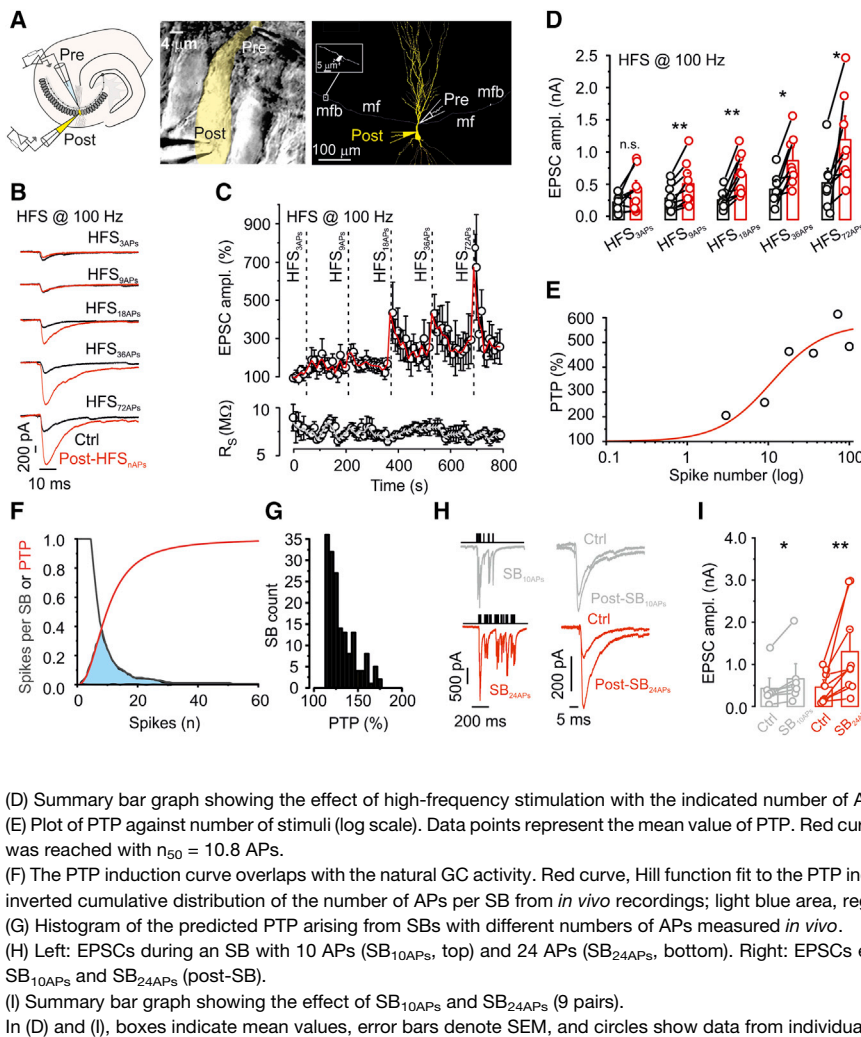
Figure 2. A Highly Sensitive Induction Mechanism of Hippocampal Mossy Fiber PTP

(A) Left: schematic illustration of the paired recording configuration (cell-attached recording from a presynaptic terminal, whole-cell recording from a postsynaptic CA3 pyramidal neuron). Center: representative differential interference contrast videomicrograph of a mossy fiber terminal-CA3 pyramidal neuron pair. The light-yellow area represents the 2D projection of the soma and proximal dendrite of the postsynaptic CA3 pyramidal neuron. Right: Neurolucida reconstruction of a mossy fiber terminal-CA3 pyramidal neuron pair. The mossy fiber terminal and axon are depicted in white, and the pyramidal neuron is shown in yellow. The inset shows an adjacent non-recorded terminal at higher magnification. Note that mossy fiber terminals were more than 100 μm apart; thus, transmitter release originates from the recorded presynaptic terminal.

(B) Average EPSCs before (black traces) and 20 s after (red traces) HFS with different numbers of stimuli, as indicated (HFS$_{3APs}$, HFS$_{9APs}$, HFS$_{18APs}$, HFS$_{36APs}$, and HFS$_{72APs}$), all at a frequency of 100 Hz.

(C) Plot of average EPSC peak amplitude (top) and postsynaptic series resistance (bottom) against experimental time. Red and gray lines indicate running averages. Vertical dashed lines indicate time points of HFS. Data are from 9 pairs.

(D) Summary bar graph showing the effect of high-frequency stimulation with the indicated number of APs on the amplitude of unitary mossy fiber EPSCs.

(E) Plot of PTP against number of stimuli (log scale). Data points represent the mean value of PTP. Red curve, Hill function fit to the data points. Half-maximal PTP was reached with $n_{50} = 10.8$ APs.

(F) The PTP induction curve overlaps with the natural GC activity. Red curve, Hill function fit to the PTP induction data and normalized to maximum; black curve, inverted cumulative distribution of the number of APs per SB from *in vivo* recordings; light blue area, region of overlap between the two curves.

(G) Histogram of the predicted PTP arising from SBs with different numbers of APs measured *in vivo*.

(H) Left: EPSCs during an SB with 10 APs (SB$_{10APs}$, top) and 24 APs (SB$_{24APs}$, bottom). Right: EPSCs evoked by single stimuli before (control) and 20 s after SB$_{10APs}$ and SB$_{24APs}$ (post-SB).

(I) Summary bar graph showing the effect of SB$_{10APs}$ and SB$_{24APs}$ (9 pairs).

In (D) and (I), boxes indicate mean values, error bars denote SEM, and circles show data from individual experiments. *p < 0.05, **p < 0.01.

High-frequency extracellular stimulation of multiple mossy fiber inputs, typically by trains of 100 pulses at a frequency of 100 Hz (HFS$_{100APs}$), is a widely used paradigm for induction of mossy fiber PTP (Griffith, 1990; Langdon et al., 1995; Salin et al., 1996; Toth et al., 2000). However, our results indicate that the natural activity of GCs is substantially more restricted. First, the low spiking frequency of GCs implies that, among the mossy fiber inputs converging on a single CA3 pyramidal neuron (~50; Amaral et al., 1990), only a single mossy fiber synapse will be active at any point in time. Second, the number of APs per SB is significantly smaller than in the HFS$_{100APs}$ protocol. To test whether *in vivo*-like activity in a single presynaptic terminal is sufficient to induce PTP, we made paired recordings between mossy fiber terminals and postsynaptic CA3 pyramidal neurons (Figure 2). Single presynaptic terminals were minimally invasively stimulated in the tight-seal, cell-attached voltage-clamp configuration (Bischofberger et al., 2006; Vyleta and Jonas, 2014; Vyleta et al., 2016), and excitatory postsynaptic currents (EPSCs) were recorded in postsynaptic CA3 pyramidal neurons in the whole-cell voltage-clamp configuration (Brown and Johnston, 1983; Figure 2A).

To determine the threshold for PTP induction, we applied trains of 3, 9, 18, 36, and 72 stimuli to single presynaptic terminals, all at a frequency of 100 Hz (Figures 2B and 2C). Although trains of three stimuli (HFS$_{3APs}$) did not significantly change the EPSC amplitude, and trains of nine stimuli (HFS$_{9APs}$) had only subtle effects, trains of 18, 36, and 72 stimuli (HFS$_{18APs}$, HFS$_{36APs}$, and HFS$_{72APs}$, respectively) induced robust PTP (300.1% ± 58.1%, 258.9% ± 62.7%, and 668.5% ± 462%, respectively; 9 mossy fiber terminal-CA3 pyramidal neuron paired recordings; p = 0.007, 0.0117, and 0.0171, respectively; Figure 2D). PTP induced by HFS$_{72APs}$ was only slightly different from that induced by HFS$_{100APs}$ in isolation (432.5% ± 73.9%; 12 pairs; p = 0.025), arguing against cumulative effects in the paradigm. Similarly, trains of 18 stimuli induced robust PTP at near-physiological temperature (Figures S1A –S1C).

To quantify the overlap between PTP induction and natural action potential (AP) activity, we plotted the magnitude of PTP against the number of stimuli during induction. We fit the dependence of PTP on AP number with a Hill equation (Figure 2E) and compared the resulting curve with the distribution of the number of APs per SB *in vivo* (Figure 2F). Consistent with the
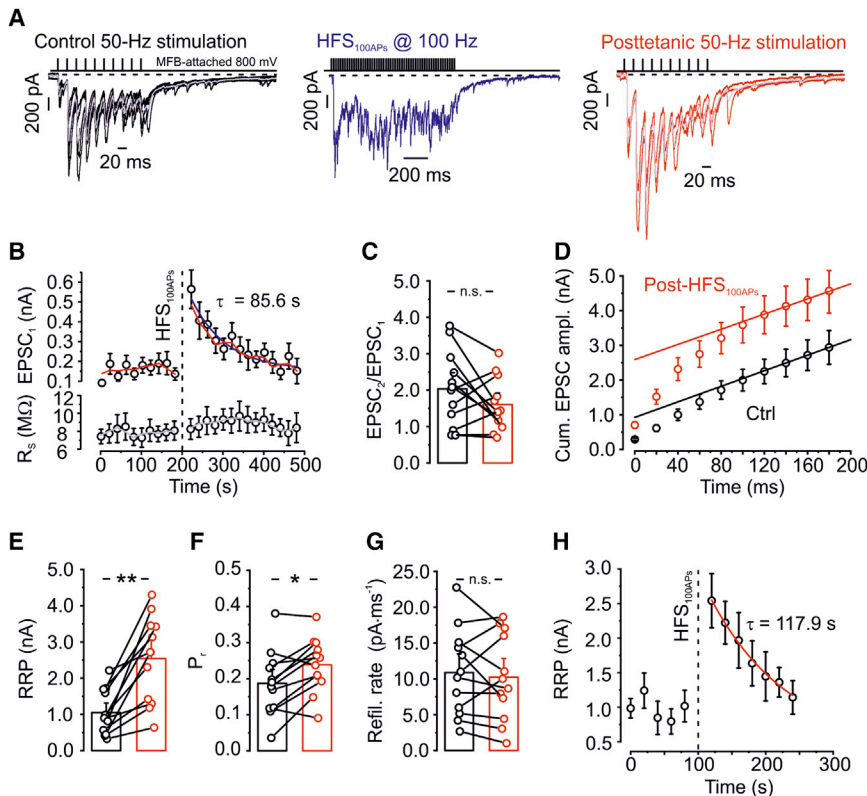
Figure 3. PTP of Mossy Fiber Unitary EPSCs Is Primarily Generated by an Increase in the Size of the RRP

(A) EPSCs evoked by a test train of 10 stimuli at 50 Hz (black), EPSCs during HFS_{100APs} (blue), and EPSCs evoked by a test train of 10 stimuli at 50 Hz 20 s after HFS_{100APs} (red).

(B) Plot of average EPSC peak amplitude (top) and postsynaptic series resistance (bottom) against experimental time. The red line represents an exponential function fit to the data points, and gray line represents running average. The vertical dashed line indicates time point of HFS_{100APs}. Data are from 12 pairs.

(C) Summary of the paired-pulse ratio ($EPSC_2$/$EPSC_1$) before (black) and after HFS_{100APs} (red). Note that the ratio was only slightly reduced after HFS_{100APs} (p = 0.158).

(D) Cumulative EPSC peak amplitude during a train with 10 stimuli at 50 Hz before (black) and 20 s after application of HFS_{100APs} (red). Data points during the last 3–5 stimuli (at time points $\geq$ 100–140 ms) were fit by linear regression. Note that PTP markedly increased the size of the RRP (represented by the intersection of the regression line with the ordinate).

(E–G) Summary bar graphs of RRP (E), P_r (F), and refilling rate (G) estimated by the 10-AP paradigm before (black) and 20 s after HFS_{100APs} (red). Bars represent mean values, error bars indicate SEM, and circles show data from individual experiments; data points from the same experiment are connected by lines. Note that PTP is caused by a preferential increase in RRP.

(H) Plot of RRP against experimental time.

physiological significance of PTP, the two curves showed marked overlap. Furthermore, quantitative analysis indicated that SBs recorded *in vivo* in identified GCs induced PTP with an average magnitude of 129% (range, 113%–176%; Figure 2G). To corroborate this conclusion, we directly applied experimentally recorded SB patterns as stimuli in paired mossy fiber terminal-CA3 pyramidal neuron recordings at near-physiological temperature (Figures 2H and 2I). Although SBs with 10 APs induced small but significant PTP, SBs with 24 APs induced marked PTP (9 pairs, p = 0.02 and 0.007, respectively; Figures 2H and 2I). Similarly, SBs with 24 APs induced robust PTP at near-physiological temperature with a near-physiological extracellular Ca^{2+} concentration (Rancz et al., 2007; Borst, 2010; Figures S1G–S1I). Taken together, natural activity patterns of identified GCs are sufficient to induce PTP at single hippocampal mossy fiber synapses.

PTP Is Mainly Generated by an Increase in RRP Size
Next we addressed the biophysical mechanisms underlying PTP at hippocampal mossy fiber synapses. In the calyx of Held, a synapse in the auditory brain stem in which PTP has been well characterized, PTP is mainly caused by a rise in the release probability (P_r) for each vesicle (Habets and Borst, 2005; Korogod et al., 2005; Fioravante et al., 2011). However, changes in the size of the RRP have also been reported (Habets and Borst, 2007; Lee et al., 2008, 2010; Chu et al., 2014). To determine the biophysical

mechanisms underlying PTP, we analyzed cumulative EPSC peak amplitudes during 50-Hz test trains of 10 stimuli applied every 20 s (Schneggenburger et al., 1999; Neher, 2015), just below the threshold for PTP induction (Figure 3). Cumulative EPSC peak amplitude was plotted against stimulus number, and data were analyzed by linear regression of the last 3–5 data points (Schneggenburger et al., 1999; Neher, 2015). The size of the RRP was determined as the intersection of the regression line with the ordinate, P_r was measured as the ratio of the first EPSC amplitude over RRP size, and the refilling rate was obtained from the slope of the regression line (Figure S2A).

We then measured RRP and P_r before and after PTP induction (Figures 3D–3H). In contrast to our expectations (Habets and Borst, 2005; Korogod et al., 2005), we found that PTP was largely mediated by an increase in RRP size. At a time point 20 s after HFS_{100APs}, the RRP markedly increased from 1048.7 ± 204.4 pA during pre-HFS periods to 2541.4 ± 355.6 pA during post-HFS periods (12 pairs, p = 0.002; Figures 3D and 3E). In contrast P_r increased only slightly, from 0.19 ± 0.03 pre-HFS to 0.24 ± 0.03 post-HFS (p = 0.015; Figures 3D and 3F). Furthermore, the refilling rate during the test train was unchanged (10.9 ± 1.8 pA × ms^{-1} pre-HFS versus 10.3 ± 1.8 pA × ms^{-1} post-HFS, p = 0.38; Figures 3D and 3G). Consistent with the hypothesis that PTP was generated by a change in RRP rather than P_r, PTP was associated with only a nonsignificant decline in the paired-pulse ratio (p = 0.158; Figure 3C). Additionally, in plots of RRP, P_r, and refilling
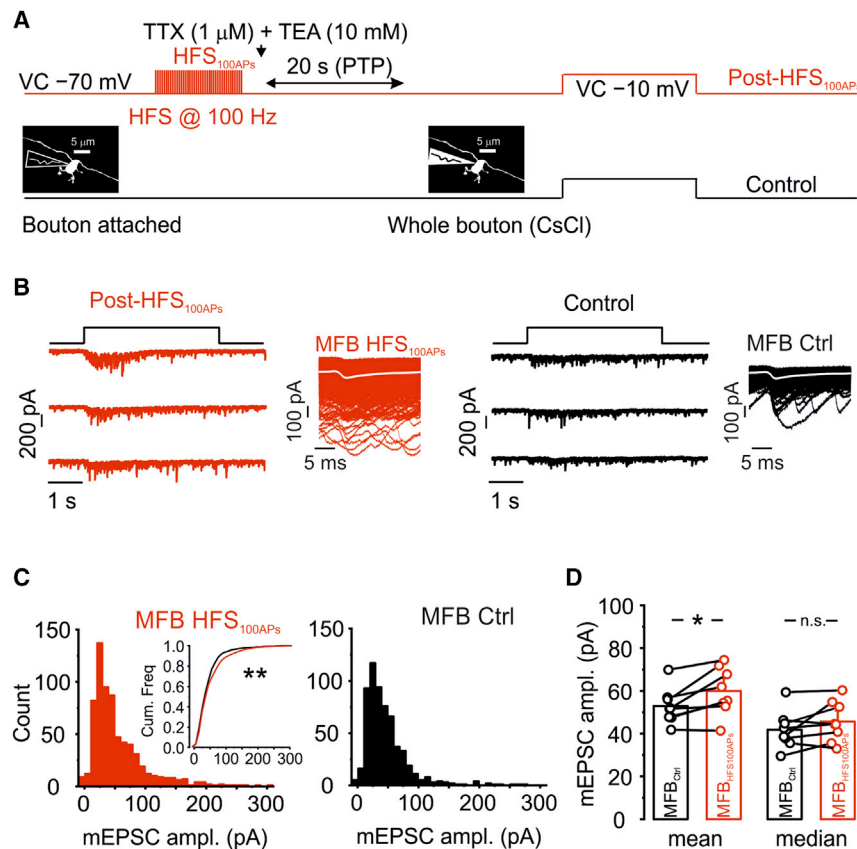
A

B

C

D

Figure 4. Increase in Q Contributes Only Minimally to Mossy Fiber PTP

(A) Schematic illustration of the experimental approach to measure mEPSCs generated by a single presynaptic mossy fiber terminal. (1) The synapse was first examined in the paired recording configuration, with the presynaptic terminal in the tight-seal, cell-attached configuration. (2) To induce PTP, the presynaptic terminal was then stimulated using HFS_{100APs} (100 stimuli at 100 Hz). (3) To enable recording of mEPSCs, TTX and TEA were applied immediately after HFS_{100APs}, and a transition was made from bouton-attached to whole-bouton configuration. (4) mEPSCs were evoked by depolarization of the presynaptic terminal with 4-s pulses from −70 mV to −10 mV. The first depolarizing pulse was applied ∼20 s after HFS. The effect of TTX was verified by the absence of Na^+ inward currents in the presynaptic terminals.

(B) Traces of mEPSCs evoked by 4-s depolarizations after HFS_{100APs} (left) and under control conditions (right). The insets show mEPSCs at an expanded timescale after detection and alignment to the onset time point; the white curve represents the average.

(C) Histograms of mEPSC peak amplitude in the same paired recordings as shown in (B). The inset shows an overlay of the corresponding cumulative distributions.

(D) Summary bar graph of the peak amplitude of mEPSCs evoked by 4-s pulses under control conditions (black) and after HFS_{100APs} (red). Note that the mean value was significantly higher (left), whereas median values were not significantly different (right), indicating a change in the shape of the distribution and a preferential increase in the proportion of large mEPSCs. Data are from 7 pairs. Boxes indicate mean values, and error bars denote SEM.

$*p < 0.05$, $**p < 0.01$.

rate against experimental time, only the change in RRP closely followed the time course characteristic for PTP (Figure 3H).

To test whether changes in quantal size (Q) contributed to PTP, we measured miniature EPSCs (mEPSCs) before and after PTP induction (Figure 4). After PTP had been induced by HFS_{100APs} in the presynaptic tight-seal, cell-attached stimulation, 1 μM tetrodotoxin (TTX) and 10 mM tetraethylammonium (TEA) were applied to the bath. After transition into the presynaptic whole-cell configuration, low-amplitude pulses were applied to the presynaptic terminal to induce mEPSCs (Figures 4A and 4B). In a time interval 20–60 s after HFS_{100APs}, the mean EPSC peak amplitude was slightly but significantly increased in comparison with later periods (59.9 ± 4.2 pA versus 52.9 ± 3.2 pA, 7 pairs, p = 0.017; Figures 4C and 4D). However, the median EPSC peak amplitude was not significantly changed, indicating an increase in the proportion of larger events (45.7 ± 3.6 pA versus 41.8 ± 3.3 pA, p = 0.12; Figure 4D). Thus, an increase in Q contributes only minimally to hippocampal mossy fiber PTP.

The validity of our analysis was confirmed by several additional tests. First, estimates of RRP were largely independent of the fitting range used for linear regression in the cumulative EPSC analysis (Figures S2B–S2G). Second, similar conclusions were reached in the presence of 1 mM of the low-affinity competitive antagonist kynurenic acid, excluding that saturation or

desensitization of postsynaptic α-amino-3-hydroxy-5-methyl-4-isoxazolepropionic acid (AMPA) receptors confounded our measurements (Habets and Borst, 2005; Figure S3). Third, analysis with an alternative method that assumes that the refilling rate depends on prior release of synaptic vesicles (Thanawala and Regehr, 2013) gave similar conclusions (Figures S4A–S4C). Fourth, similar conclusions were obtained at reduced and increased extracellular Ca^{2+} concentrations (1.2 mM and 4 mM, respectively; Figure S5). Additionally, these results directly demonstrate that PTP-induced changes in RRP are largely independent of Ca^{2+} concentration-related changes in P_r. Finally, analysis with a model containing three vesicle pools (docked, primed, and superprimed pool; Lee et al., 2013; Taschenberger et al., 2016) confirmed that the size of the RRP was increased after PTP (Figures S4D–S4F). Taken together, these results converge on the conclusion that PTP at the hippocampal mossy fiber synapse was primarily mediated by an increase in the size of the RRP.

PTP Is Associated with an Increase in the Docked Vesicle Pool

According to our results, PTP was generated by an increase in RRP size. Such an increase may arise from changes in vesicle docking, priming, or both (Imig et al., 2014). To distinguish
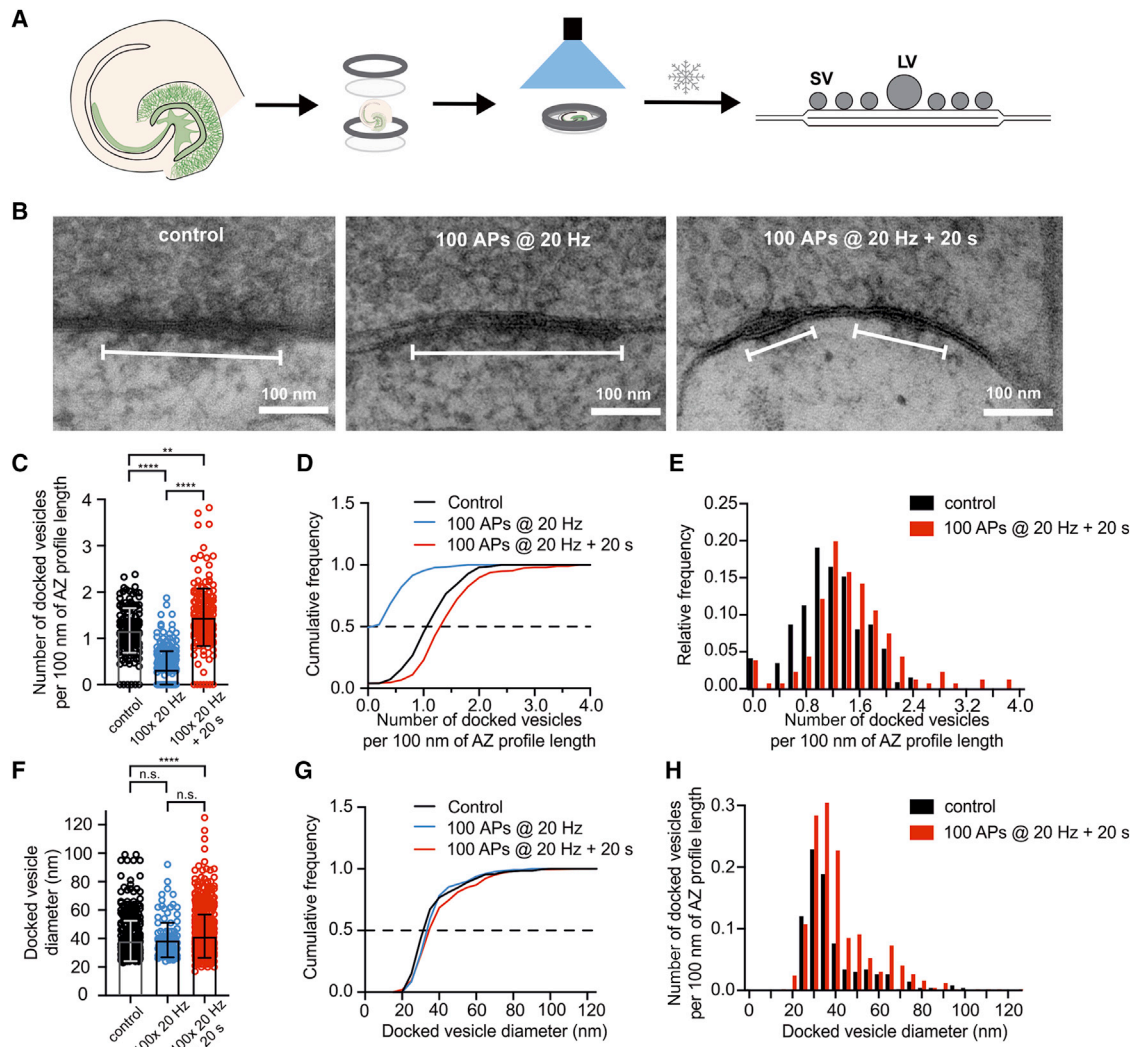
Figure 5. Functional EM Analysis Reveals an Increase in the Number of Docked Vesicles during PTP

(A) Left: schematic illustration of "flash and freeze" experiments at hippocampal mossy fiber synapses. Thin hippocampal slices were embedded in a sandwich between two sapphire blades, hippocampal GCs were stimulated by light pulses, and slices were subjected to high-pressure freezing at defined time intervals for subsequent EM analysis (Borges-Merjane et al., 2020).

(B) Example transmission EM (TEM) micrographs of active zones of hippocampal mossy fiber synapses in control slices (left), slices frozen immediately after stimulation with 100 light pulses (center), and slices frozen 20 s after stimulation (right). Images were taken from the mossy fiber tract in the *stratum lucidum* of the CA3 region, primarily CA3b and CA3c.

(C–E) Scatterplot (C), cumulative distributions (D), and histograms (E) of the number of docked vesicles per 100 nm of active zone profile length for a non-light stimulated control (black), slices frozen immediately after HFS_{100APs} stimulation at 20 Hz (blue), and slices frozen after HFS_{100APs} stimulation + 20 s recovery time (red). Bars show mean and standard deviation. Each data point in (C) represents an active-zone profile. Note that the number of docked vesicles increased 20 s after HFS, indicating "overfilling" of the docked vesicle pool.

(F–H) Similar plots as shown in (C)–(E) but for diameter of docked vesicles. The diameter of docked vesicles was slightly but significantly larger in the HFS_{100APs} stimulation + 20 s recovery time in comparison with control experiments. Each data point in (F) represents a docked synaptic vesicle. Data for the HFS_{100APs} stimulation (blue) include measurements taken from a previous study (Borges-Merjane et al., 2020).

In (C) and (F), boxes indicate mean values, and error bars denote standard deviation. **p < 0.01, ****p < 0.0001.

between these possibilities, we performed functional EM ("flash and freeze") experiments at hippocampal mossy fiber synapses (Watanabe et al., 2013a, 2013b; Borges-Merjane et al., 2020; Figure 5). GCs in acute slices were targeted for optogenetic stimulation using prospero homeobox 1 (Prox1)-CreER[T2] × channelrhodopsin ChR2(H134R)-enhanced yellow fluores-

cent protein (EYFP) mice (STAR Methods; Borges-Merjane et al., 2020). To mimic the HFS induction protocol used in the electrophysiological experiments, 100 stimuli were applied at the highest possible frequency at which reliable channelrhodopsin stimulation could be achieved (20 Hz). At defined time points after optical stimulation, acute slices were subjected to

high-pressure freezing and subsequently processed for EM analysis (Figures 5A and S6). Mossy fiber terminals were identified based on location in the *stratum lucidum*, large size, termination on thorny excrescences of CA3 pyramidal cells, and high density of synaptic vesicles (Chicurel and Harris, 1992; Rollenhagen et al., 2007; Borges-Merjane et al., 2020).

In unstimulated control slices, the number of docked vesicles (within 5 nm of the plasma membrane) was 1.16 ± 0.04 per 100-nm active zone profile length (mean $\pm$ standard deviation, 154 profiles, 4 mice; Figures 5B–5E), consistent with previous measurements (Rollenhagen et al., 2007). When slices were frozen immediately after HFS_{100APs}, the number of docked vesicles was strongly reduced to 0.33 ± 0.03 per 100-nm active zone profile length ($p < 0.0001$, 234 profiles, 3 mice; Figures 5C and 5D, blue symbols and lines), as reported previously (Borges-Merjane et al., 2020). This was consistent with a model in which synaptic vesicles at hippocampal mossy fiber synapses underwent full fusion. When slices were frozen 20 s after HFS_{100APs}, the number of docked vesicles was 1.45 ± 0.04 per 100-nm active zone profile length (193 profiles, 4 mice; Figures 5C–5E, red symbols and lines). Thus, the number of docked vesicles per profile was not only markedly higher than directly after HFS ($p < 0.0001$) but also significantly larger than under control conditions ($p = 0.003$; Figures 5C–5E).

On average, the number of docked vesicles per profile 20 s after HFS was 1.243 times larger than in interleaved control experiments. Because the number of vesicles per active zone (measured in 2 dimensions) is quadratically related to the number of vesicles per profile (measured in 1 dimension; Figure S6D), we estimate that the number of docked vesicles per active zone was increased by a factor of $(1.243)^2 = 1.545$. To further corroborate that PTP was evoked in our "flash and freeze" experiments, we measured the effects of optogenetic HFS_{100APs} at 20 Hz in electrophysiological experiments under identical conditions (Figures S6A and S6B). Optogenetic HFS_{100APs} induced significant PTP (5 CA3 pyramidal neuron recordings), although the magnitude was smaller ($207\% \pm 39\%$) than with electrical HFS_{100APs} ($432\% \pm 73\%$, $p = 0.02$; Figure 3B). Taken together, the increase in the RRP after HFS (Figure 3) can be largely explained by an increase in the number of docked vesicles.

Detailed analysis of electron micrographs revealed that the mean diameter of docked vesicles was also slightly but significantly increased 20 s after HFS, from 37.7 ± 0.8 nm under control conditions to 43.8 ± 1.1 nm 20 s after HFS (Figures 5F–5H). Because larger vesicles might release a higher amount of glutamate, this may explain the additional increase in mean mEPSC amplitude observed in our paired recording experiments (Figure 4D). Thus, HFS_{100APs} led to a marked increase in the number of docked vesicles and a slight increase in their mean diameter.

Pool Refilling Determines PTP
PTP increased the size of the RRP, implying that pool refilling is a major determinant of short-term plasticity. To further test this hypothesis, we reciprocally examined the relation between refilling rate and PTP (Figure 6). First, we tested whether pharmacological manipulations that affected PTP also changed the refilling rate. Because PTP at the hippocampal mossy fiber synapse is known to involve the cyclic AMP (cAMP)-protein kinase A

(PKA) pathway (Weisskopf et al., 1994; Alle et al., 2001), we examined the effects of the PKA blocker H-89 (Figures 6A–6C). Surprisingly, we found that 10 μM H-89 reduced the EPSC amplitude under control conditions from 342.3 ± 33.6 pA to 61.6 ± 21.6 pA after 380 s of application of the drug ($p = 0.0179$; Figures 6A and 6B). As expected, subsequent HFS_{100APs} applied in the presence of H-89 had no additional effects on EPSC amplitude ($p = 0.176$; Figures 6A and 6B). These results suggest that PKA regulates basal transmission and PTP induction. To determine the underlying mechanisms, we analyzed cumulative EPSC amplitude during HFS_{100APs} under control conditions and in the presence of H-89 (Figures 6C and 6E). H-89 only slightly reduced the size of the RRP (from $1,862.7 \pm 407.3$ pA to $1,599 \pm 294$ pA) and left P_r unchanged (0.104 ± 0.031 versus 0.086 ± 0.030, 7 pairs, $p = 0.50$). However, H-89 substantially decreased the refilling rate during HFS_{100APs} (from 7.97 ± 1.27 pA $\times$ ms^{-1} to 2.53 ± 0.62 pA $\times$ ms^{-1}, $p = 0.004$; Figures 6C and 6E). Thus, PKA block abolished PTP and, in parallel, reduced the pool refilling rate during HFS_{100APs}.

Next we examined whether the pharmacological manipulations that affected refilling also changed PTP. At the calyx of Held and cerebellar parallel fiber-interneuron synapses, pool refilling is dependent on an intact actin cytoskeleton (Sakaba and Neher, 2003; Miki et al., 2018). Thus, we tested the effects of the actin polymerization inhibitors latrunculin B and cytochalasin D (Figures 6D–6G). As expected from the results from the calyx of Held, 20 μM latrunculin B and 10 μM cytochalasin D reduced refilling rate during HFS_{100APs} from 7.97 ± 1.27 pA·ms^{-1} to 4.3 ± 0.84 pA·ms^{-1} ($p = 0.025$; Figures 6D and 6E). In parallel, latrunculin B and cytochalasin D attenuated PTP (from $432\% \pm 74\%$ under control conditions to $136\% \pm 38\%$ in the presence of polymerization inhibitors ($p = 0.003$, 8 pairs; Figures 6F–6H). To further test the hypothesis that PTP is generated by pool refilling during HFS, we plotted the magnitude of PTP after HFS_{100APs} for all datasets (under control conditions, in the presence of H-89, and in the presence of latrunculin B and cytochalasin D) against the refilling rate during HFS_{100APs} (Figure 6I). The magnitude of PTP was highly correlated with the refilling rate during HFS_{100APs} (Spearman rank correlation coefficient $\rho = 0.61$, $p = 0.0005$, 28 pairs; Figure 6I). Taken together, these results corroborate the hypothesis that vesicle pool refilling underlies PTP. This conclusion was further supported by our three-pool model with activity-dependent refilling, which closely replicated our experimental datasets before, during, and after PTP induction (Figures S4D–S4F). In summary, these results indicate that PTP is generated by enhanced vesicle refilling during HFS.

Extended Time Course of Potentiation in Delay Paradigms
If PTP has physiological significance, then conditions for induction and readout must be satisfied. Thus, single spikes or bursts must follow SBs and fall into the time window of PTP. To test whether this condition occurs, we quantified the likelihood of SB-single spike and SB-burst sequences in our *in vivo* dataset (Figures 7A–7E). SBs were more frequently followed by a single spike (55%) than by a burst (10%) or a second SB (30%) (Figure 7A). The latency between an SB and subsequent events,
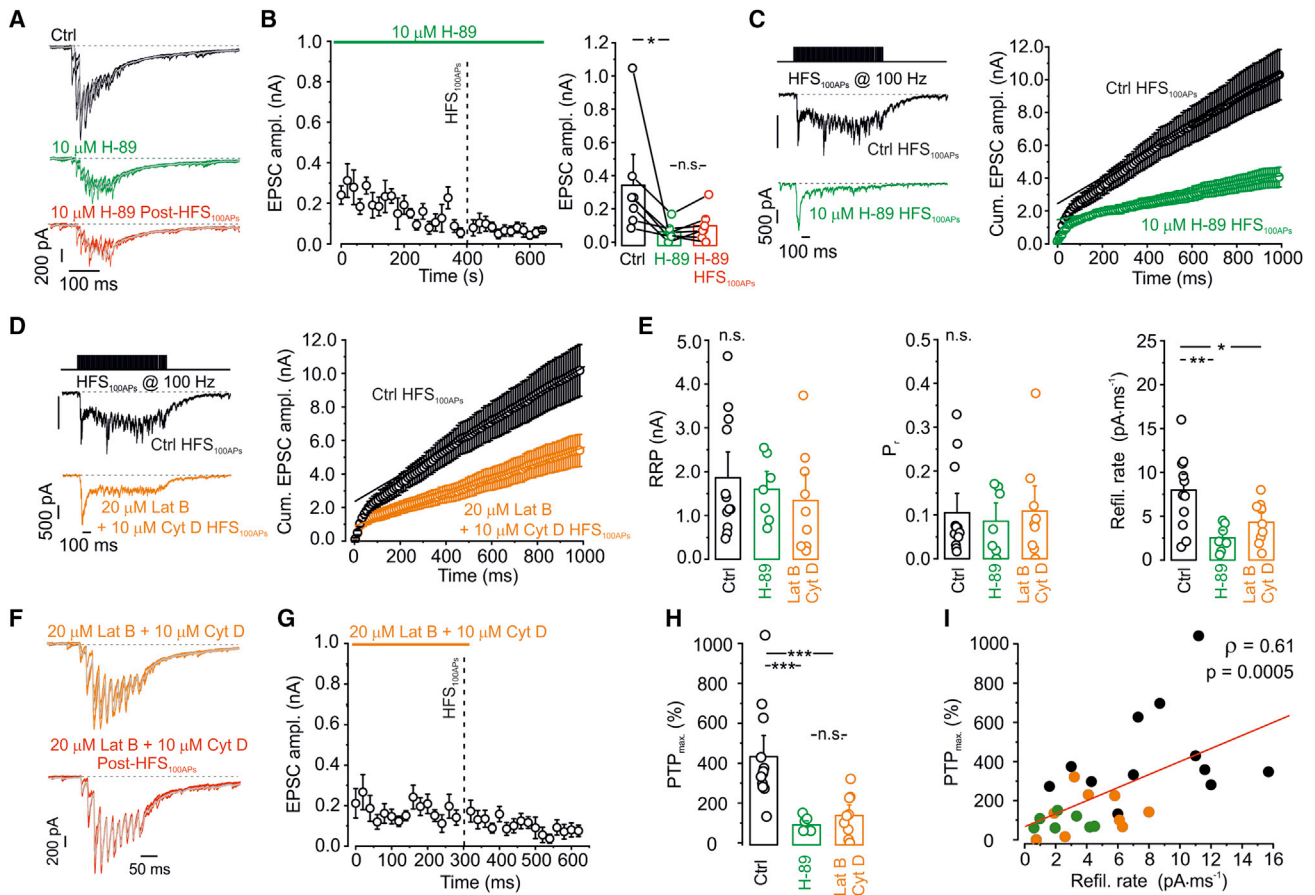
Figure 6. Pool Refilling Rate during HFS$_{100APs}$ Predicts the Magnitude of PTP

(A–C) The PKA blocker H-89 (10 μM) inhibits PTP and pool refilling.

(A) Unitary EPSCs evoked by a train of 10 stimuli in the presynaptic terminal before application of H-89 (black), in the presence of H-89 before HFS$_{100APs}$ (green), and in the presence of H-89 after HFS$_{100APs}$ (red).

(B) Left: plot of EPSC$_1$ against experimental time. H-89 was applied during the horizontal green continuous line, and HFS$_{100APs}$ was applied at the time point indicated by the vertical black dashed line. Note that H-89 reduced EPSC$_1$ peak amplitude and suppressed the induction of PTP after subsequent HFS$_{100APs}$. Right: summary bar graph. Data are from 7 pairs.

(C) Left: unitary EPSCs evoked by HFS$_{100APs}$ under control conditions (black) and in the presence of H-89 (green). Right: plot of cumulative EPSC peak amplitude (100 stimuli, 100 Hz in presynaptic cell-attached stimulation) under control conditions (black) and in the presence of H-89 (green).

(D) Similar plots as shown in (C), but with the actin polymerization blockers latrunculin B (20 μM) and cytochalasin D (10 μM). Traces from different pairs; same control trace shown in (C, left) and (D, left).

(E) Comparison of RRP (left), P$_r$ (center), and refilling rate (right) under control conditions (black), in the presence of H-89 (green), and in the presence of latrunculin B and cytochalasin D. RRP and P$_r$ were unchanged, whereas the refilling rate was significantly reduced by H-89 and the actin polymerization blockers.

(F) Unitary EPSCs evoked by a train of 10 stimuli in the presynaptic terminal in the presence of latrunculin B and cytochalasin D before (orange) and after (red) HFS$_{100APs}$.

(G) Plot of EPSC$_1$ against experimental time. Latrunculin B and cytochalasin D were applied during the horizontal orange continuous line, and HFS$_{100APs}$ was applied at the time point indicated by the vertical black dashed line. Actin polymerization blockers reduce synaptic transmission and inhibit PTP.

(H) Summary bar graph of the effects of H-89 and latrunculin B and cytochalasin D on PTP.

(I) Scatterplot of the magnitude of PTP against the refilling rate during HFS$_{100APs}$. Black, control data; green, data in the presence of H-89; orange, data in the presence of latrunculin B and cytochalasin D. The line represents linear regression to the data points (Spearman rank correlation coefficient $\rho = 0.61$, $p = 0.0005$, 28 pairs).

In (B), right, (E), and (H), boxes indicate mean values, error bars denote SEM, circles show data from individual experiments, and data from the same experiment are connected by lines. *$p < 0.05$, **$p < 0.01$, ***$p < 0.001$.

quantified on a cell-by-cell basis, was 6.0 ± 2.1 s for the first AP and 91.7 ± 34.1 s for the last AP (20 GCs; Figures 7B–7E). Thus, although the range of SB-AP intervals overlapped with the time window of PTP, a substantial proportion of latencies extended beyond this time window.

How could these late events be used for PTP readout? If PTP is mediated by an increase in the size of vesicle pools, then exocytosis may dissipate the potentiation. Conversely, the absence of activity might extend the lifetime of the "pool engram." To test this prediction, we compared PTP with two experimental
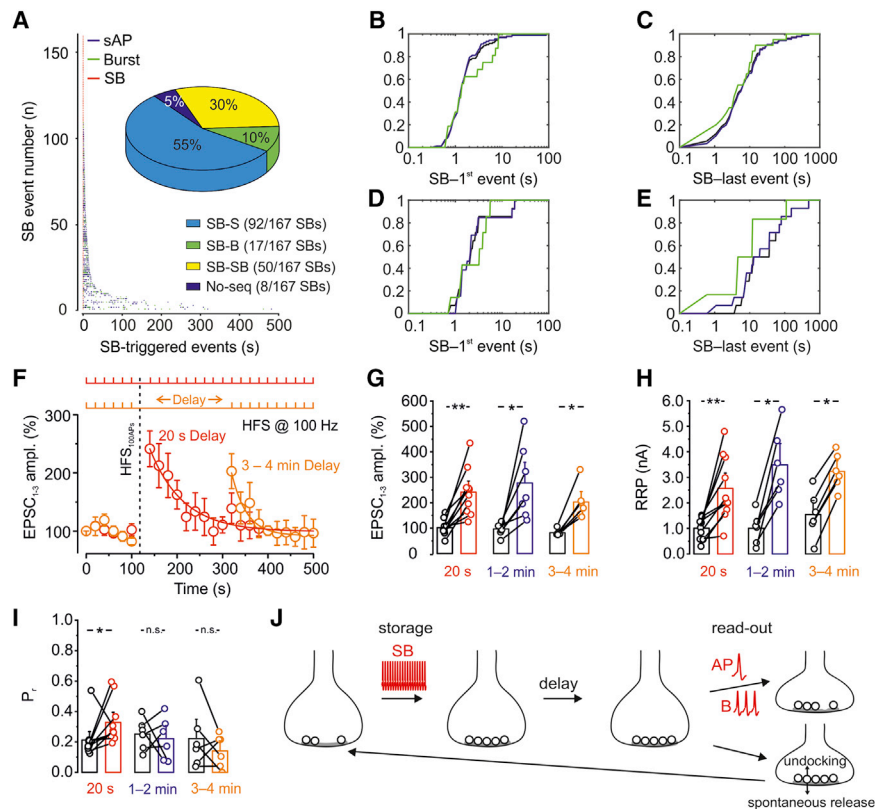
Figure 7. Long SB-Spike and SB-Burst Intervals and Extended Time Course of PTP in the Absence of Activity

(A) Left: rasterplot analysis of activity following SBs in GCs *in vivo*. Points represent activity events (blue, single APs; green, bursts; red, SBs). Events were sorted according to the time point of the last event. Note that the activity extended over several seconds in a subset of events. Inset: summary pie chart of the percentage of SB-single spike (light blue), SB-burst (green), and SB-SB sequences (yellow).

(B and C) Cumulative distributions of latencies between SBs and the first event (B) and last event (C) for all events (black), spikes (blue), and bursts (green). In total, data represent 167 SBs.

(D and E) Similar analysis as shown in (B) and (C) but for the mean latencies in individual GCs. Note that the SB-last event latency covers and occasionally exceeds the time window of PTP. In total, data were obtained from 20 GCs *in vivo*.

(F) Absence of stimulation extends the time period of PTP. Red, plot of EPSC peak amplitude against experimental time during the standard stimulation paradigm (test stimulation once every 20 s, followed by HFS$_{100APs}$, followed by test stimulation once every 20 s); orange, plot of EPSC peak amplitude against time during a stimulation paradigm with a 3- to 4-min delay period. The inset shows test stimulation, and the vertical dashed line indicates HFS$_{100APs}$. Note that PTP was significantly larger in the delay protocol than expected for a process that exponentially decays

after HFS$_{100APs}$. Thus, the time course of PTP was extended in the absence of activity. Data were from 9 pairs (20 s) and 6 pairs (3–4 min).

(G) Comparison of PTP after HFS$_{100APs}$, with 20-s delay, 1- to 2-min delay, and 3- to 4-min delay. Data were from 9 pairs (20 s), 6 pairs (1–2 min), and 6 pairs (3–4 min).

In (F and G), PTP was quantified from the amplitudes of the first three EPSCs.

(H and I) Similar plots as in (G) but for RRP (H) and P_r (I). Note that, after a delay, PTP was generated by a selective increase in RRP.

(G–I) Boxes indicate mean values, and error bars denote SEM. *p < 0.05, **p < 0.01.

(J) Pool engrams may allow prolonged storage and efficient readout of information in hippocampal circuits. Natural GC activity (SBs) increases the docked vesicle pool, leading to a structural "pool engram." In the absence of activity ("delay"), the pool engram is long lasting. APs or bursts can lead to readout of information after a delay. The lifetime of the pool engram is limited by the readout (right top) or by the rates of spontaneous release and vesicle undocking (right bottom; Murthy and Stevens, 1999).

---

protocols: the standard protocol, in which test pulses directly followed HFS$_{100APs}$ with a 20 s repetition rate, and an alternative protocol, in which test pulses followed HFS$_{100APs}$ after a delay of 1–5 min (Figure 7F). Lack of activity during the delay period was verified by the absence of action currents in the presynaptic terminal. For the standard protocol, PTP had a magnitude of 241% and decayed with a time constant of 81 s. If PTP decayed with uniform time course after induction, then it should have decayed to 107% after a 4-min delay period. However, in contrast to this prediction, we found that PTP after 3–4 min was similar to that probed immediately after HFS$_{100APs}$ (245% ± 23% versus 241% ± 31%, 6 pairs, p = 0.97; Figures 7F and 7G). After the delay, the selective reliance of PTP on RRP size changes (Figure 3) was further enhanced, with significant changes in RRP but no changes in P_r (Figures 7H and 7I). Thus, the time course of PTP was extended in the complete absence of presynaptic activity. The sparse and patterned activity of GCs is ideally suited to use this mechanism. Although the generation of SBs guarantees efficient storage of information, the long SB-AP time interval enables reliable readout (Figure 7J).

DISCUSSION

Our results provide compelling evidence of physiological relevance of PTP. First, *in vivo* recordings identify SBs as a novel form of patterned activity of GCs. Second, PTP at hippocampal mossy fiber synapses shows a low induction threshold. Thus, the PTP induction curve and the distribution of APs in SBs overlap. Finally, SBs are often followed by single APs. Taken together, the natural activity patterns of GCs are not only highly suitable for induction of PTP but also for efficient readout.

Our functional analysis shows that PTP is mediated by enlargement of the RRP (Figure S7A). This implies that PTP requires pool refilling during or after HFS. This hypothesis is further corroborated by the effects of PKA blockers and actin polymerization inhibitors, which reduce refilling and PTP in parallel. An attractive molecular mechanism that links the effects of PKA and actin may involve synapsins. In this model, phosphorylation may enhance pool refilling by dissociating synaptic vesicles from the actin cytoskeleton (Gitler et al., 2008; Patzke et al., 2019; reviewed by Cingolani and Goda, 2008). A large reserve pool may

be needed to ensure fast and sustained reloading of the RRP at multiple active zones. Thus, the model attributes a function to the large vesicle pool in mossy fiber terminals (Chicurel and Harris, 1992; Rollenhagen et al., 2007), which has puzzled researchers for decades.

Although PTP predominantly increases the RRP, other forms of mossy fiber plasticity are well known to change P_r (that is, the fusion probability per vesicle) through AP broadening (Geiger and Jonas, 2000), buffer saturation (Vyleta and Jonas, 2014), and tightening of Ca^{2+} channel-sensor coupling (Midorikawa and Sakaba, 2017; Jackman and Regehr, 2017; Figure S7B). Thus, the mossy fiber synapse is endowed with orthogonal forms of plasticity, which may interact multiplicatively. However, this scheme is a simplification because, according to our results, multiple mechanisms contribute to PTP (increase in RRP, P_r, and Q). Thus, changes in RRP and Q representing a major component of PTP will multiplicatively interact with changes in P_r, reflecting a minor component of PTP and other plasticity forms. In combination, these changes enrich the repertoire of single-synapse computations (Abbott and Regehr, 2004; Silver, 2010; Henze et al., 2002; Vyleta et al., 2016; Chamberland et al., 2018). Although an increase in P_r may lead to a burst-to-spike transmission mode, an increase in RRP could facilitate a burst-to-burst transmission regime (Vyleta et al., 2016). Such a transmission mode may explain the prevalence of bursting in CA3 pyramidal neurons *in vivo* (Kowalski et al., 2016).

Our results reveal that structural changes are associated with short-term plasticity. Although structural changes during presynaptic plasticity have been reported in invertebrate synapses (for example, *Aplysia*; Bailey et al., 2015), such changes have not been identified in mammalian synapses. It is widely thought that PTP is caused by an increase in Ca^{2+} concentration and an associated increase in P_r (Regehr et al., 1994; Zucker and Regehr, 2002; Habets and Borst, 2005; Korogod et al., 2005). However, such changes may be too short-lasting to contribute to short-term memory. Our functional EM ("flash and freeze") experiments reveal that the number of docked vesicles increases 20 s after HFS_{100APs} stimulation at 20 Hz. In the absence of activity, the increase in the docked vesicle pool seems to have a markedly prolonged lifetime. This may be related to the low rates of spontaneous release and vesicle undocking (Murthy and Stevens, 1999). The long lifetime of the pool engram may be explained by the energetics of the SNAP receptor (SNARE) complex (consisting of syntaxin, SNAP-25, and synaptobrevin). In docked or primed vesicles, SNARE complexes may be partially zippered, leading to an almost irreversible reaction toward exocytosis (Fasshauer et al., 2002). This suggests that the SNARE complex not only provides the energy for membrane fusion but also implements a molecular mechanism for information storage. Thus, exocytosis and synaptic plasticity might be more intimately linked than previously thought.

Our findings suggest that PTP mediated by a vesicle pool mechanism is suitable for short-term storage of information in the hippocampus (Squire and Zola-Morgan, 1991). First, PTP shows a long decay time course that is further extended in the absence of activity. Additionally, the time course of potentiation may be prolonged by neuromodulators (Huang and Kandel, 1996). Thus, the time course of PTP approaches that of hippocampal short-term memory (Squire and Zola-Morgan, 1991; Deadwyler et al., 1996). Second, the pool mechanism of PTP is energetically efficient. Although the maintenance of enlarged vesicle pools does not consume any energy, persistent AP generation requires an ongoing energy supply (Attwell and Laughlin, 2001). Third, pool mechanisms may be particularly suitable for storage of information in the dentate gyrus-CA3 circuit, in which sparse activity prevails (Pernía-Andrade and Jonas, 2014; Pilz et al., 2016; X.Z., A. Schlögl, and P.J., unpublished data; Figure 1). Pool mechanisms may be particularly useful during delayed nonmatch-to-sample tasks, in which neurons often show high activity in sample or test phase but low activity in the delay phase (Deadwyler et al., 1996; Wiebe and Stäubli, 1999).

Classical work tried to identify engrams; that is, physical or chemical changes underlying the formation of new memories (Lashley, 1950). Does the increase in the number of docked vesicles in presynaptic terminals represent a "vesicle pool engram"? It is well established that dentate gyrus GCs participate in formation of engrams and that their reactivation is sufficient to trigger memory recall and behavioral responses (Liu et al., 2012). It has been proposed that hippocampal engram cells show enhanced excitability and a higher functional connectivity than nonengram cells (Josselyn and Tonegawa, 2020). However, the underlying physical or chemical modifications remain elusive. Our findings suggest that changes in the docked vesicle pool in mossy fiber terminals may contribute to formation of engrams. Although our results demonstrate that the PKA pathway regulates vesicle pool size, previous work indicated a link between the PKA pathway in GCs and contextual memory formation (Jones et al., 2016). Taken together, these results may suggest an intriguing connection between synaptic vesicle pools and hippocampal memory. More work is needed to rigorously test the vesicle pool engram hypothesis and close the gap between synaptic and behavioral level.

STAR★METHODS

Detailed methods are provided in the online version of this paper and include the following:

- KEY RESOURCES TABLE
- RESOURCE AVAILABILITY
  - Lead Contact
  - Materials Availability
  - Data and Code Availability
- EXPERIMENTAL MODEL AND SUBJECT DETAILS
  - Animal experiments
- METHOD DETAILS
  - *In vivo* recordings from identified dentate gyrus GCs
  - Brain slice preparation
  - Presynaptic cell-attached and whole-bouton recording
  - Postsynaptic whole-cell somatic recording
  - PTP induction protocols
  - Thin-slice preparation for functional electron microscopy
  - High-pressure freezing
  - Freeze substitution, embedding, and electron microscopy

Neuron
Article

- ● QUANTIFICATION AND STATISTICAL ANALYSIS
  - ○ Electrophysiology data analysis
  - ○ Electron micrograph analysis
  - ○ Modeling of pool dynamics
  - ○ Statistics and conventions

AUTHOR CONTRIBUTIONS

D.V. performed the *in vitro* paired recordings. C.B.-M. carried out the "flash and freeze" experiments. X.Z. conducted the *in vivo* recordings. P.J. performed modeling and wrote the paper. All authors analyzed the data and jointly revised the paper.

DECLARATION OF INTERESTS

The authors declare no competing interests.

REFERENCES

Abbott, L.F., and Regehr, W.G. (2004). Synaptic computation. Nature *431*, 796–803.

Acsády, L., Kamondi, A., Sík, A., Freund, T., and Buzsáki, G. (1998). GABAergic cells are the major postsynaptic targets of mossy fibers in the rat hippocampus. J. Neurosci. *18*, 3386–3403.

Alcami, P., Franconville, R., Llano, I., and Marty, A. (2012). Measuring the firing rate of high-resistance neurons with cell-attached recording. J. Neurosci. *32*, 3118–3130.

Alle, H., Jonas, P., and Geiger, J.R.P. (2001). PTP and LTP at a hippocampal mossy fiber-interneuron synapse. Proc. Natl. Acad. Sci. USA *98*, 14708–14713.

Alme, C.B., Buzzetti, R.A., Marrone, D.F., Leutgeb, J.K., Chawla, M.K., Schaner, M.J., Bohanick, J.D., Khoboko, T., Leutgeb, S., Moser, E.I., et al. (2010). Hippocampal granule cells opt for early retirement. Hippocampus *20*, 1109–1123.

Amaral, D.G., Ishizuka, N., and Claiborne, B. (1990). Neurons, numbers and the hippocampal network. Prog. Brain Res. *83*, 1–11.

Attwell, D., and Laughlin, S.B. (2001). An energy budget for signaling in the grey matter of the brain. J. Cereb. Blood Flow Metab. *21*, 1133–1145.

Bailey, C.H., Kandel, E.R., and Harris, K.M. (2015). Structural components of synaptic plasticity and memory consolidation. Cold Spring Harb. Perspect. Biol. *7*, a021758.

Bazigou, E., Lyons, O.T., Smith, A., Venn, G.E., Cope, C., Brown, N.A., and Makinen, T. (2011). Genes regulating lymphangiogenesis control venous valve formation and maintenance in mice. J. Clin. Invest. *121*, 2984–2992.

Bischofberger, J., Engel, D., Li, L., Geiger, J.R.P., and Jonas, P. (2006). Patch-clamp recording from mossy fiber terminals in hippocampal slices. Nat. Protoc. *1*, 2075–2081.

Bittner, K.C., Grienberger, C., Vaidya, S.P., Milstein, A.D., Macklin, J.J., Suh, J., Tonegawa, S., and Magee, J.C. (2015). Conjunctive input processing drives feature selectivity in hippocampal CA1 neurons. Nat. Neurosci. *18*, 1133–1142.

Borges-Merjane, C., Kim, O., and Jonas, P. (2020). Functional electron microscopy, "flash and freeze," of identified cortical synapses in acute brain slices. Neuron *105*, 992–1006.

Borst, J.G.G. (2010). The low synaptic release probability in vivo. Trends Neurosci. *33*, 259–266.

Brown, T.H., and Johnston, D. (1983). Voltage-clamp analysis of mossy fiber synaptic input to hippocampal neurons. J. Neurophysiol. *50*, 487–507.

Chamberland, S., Timofeeva, Y., Evstratova, A., Volynski, K., and Tóth, K. (2018). Action potential counting at giant mossy fiber terminals gates information transfer in the hippocampus. Proc. Natl. Acad. Sci. USA *115*, 7434–7439.

Chanaday, N.L., and Kavalali, E.T. (2018). Optical detection of three modes of endocytosis at hippocampal synapses. eLife *7*, e36097.

Chicurel, M.E., and Harris, K.M. (1992). Three-dimensional analysis of the structure and composition of CA3 branched dendritic spines and their synaptic relationships with mossy fiber boutons in the rat hippocampus. J. Comp. Neurol. *325*, 169–182.

Chu, Y., Fioravante, D., Leitges, M., and Regehr, W.G. (2014). Calcium-dependent PKC isoforms have specialized roles in short-term synaptic plasticity. Neuron *82*, 859–871.

Cingolani, L.A., and Goda, Y. (2008). Actin in action: the interplay between the actin cytoskeleton and synaptic efficacy. Nat. Rev. Neurosci. *9*, 344–356.

Deadwyler, S.A., Bunn, T., and Hampson, R.E. (1996). Hippocampal ensemble activity during spatial delayed-nonmatch-to-sample performance in rats. J. Neurosci. *16*, 354–372.

Efron, B., and Tibshirani, R.J. (1998). An introduction to the bootstrap (London: Chapman and Hall/CRC).

Fasshauer, D., Antonin, W., Subramaniam, V., and Jahn, R. (2002). SNARE assembly and disassembly exhibit a pronounced hysteresis. Nat. Struct. Biol. *9*, 144–151.

Fioravante, D., Chu, Y., Myoga, M.H., Leitges, M., and Regehr, W.G. (2011). Calcium-dependent isoforms of protein kinase C mediate posttetanic potentiation at the calyx of Held. Neuron *70*, 1005–1019.

Geiger, J.R.P., and Jonas, P. (2000). Dynamic control of presynaptic Ca^{2+} inflow by fast-inactivating K$^+$ channels in hippocampal mossy fiber boutons. Neuron *28*, 927–939.

Geiger, J.R.P., Melcher, T., Koh, D.S., Sakmann, B., Seeburg, P.H., Jonas, P., and Monyer, H. (1995). Relative abundance of subunit mRNAs determines gating and Ca^{2+} permeability of AMPA receptors in principal neurons and interneurons in rat CNS. Neuron *15*, 193–204.

Gitler, D., Cheng, Q., Greengard, P., and Augustine, G.J. (2008). Synapsin IIa controls the reserve pool of glutamatergic synaptic vesicles. J. Neurosci. *28*, 10835–10843.

Goldman-Rakic, P.S. (1995). Cellular basis of working memory. Neuron *14*, 477–485.

Griffith, W.H. (1990). Voltage-clamp analysis of posttetanic potentiation of the mossy fiber to CA3 synapse in hippocampus. J. Neurophysiol. *63*, 491–501.

Gundlfinger, A., Breustedt, J., Sullivan, D., and Schmitz, D. (2010). Natural spike trains trigger short- and long-lasting dynamics at hippocampal mossy fiber synapses in rodents. PLoS ONE *5*, e9961.

Guzman, S.J., Schlögl, A., and Schmidt-Hieber, C. (2014). Stimfit: quantifying electrophysiological data with Python. Front. Neuroinform. 8, 16.

Habets, R.L., and Borst, J.G.G. (2005). Post-tetanic potentiation in the rat calyx of Held synapse. J. Physiol. 564, 173–187.

Habets, R.L., and Borst, J.G.G. (2007). Dynamics of the readily releasable pool during post-tetanic potentiation in the rat calyx of Held synapse. J. Physiol. 581, 467–478.

Henze, D.A., Wittner, L., and Buzsáki, G. (2002). Single granule cells reliably discharge targets in the hippocampal CA3 network in vivo. Nat. Neurosci. 5, 790–795.

Huang, Y.Y., and Kandel, E.R. (1996). Modulation of both the early and the late phase of mossy fiber LTP by the activation of beta-adrenergic receptors. Neuron 16, 611–617.

Imig, C., Min, S.W., Krinner, S., Arancillo, M., Rosenmund, C., Südhof, T.C., Rhee, J., Brose, N., and Cooper, B.H. (2014). The morphological and molecular nature of synaptic vesicle priming at presynaptic active zones. Neuron 84, 416–431.

Jackman, S.L., and Regehr, W.G. (2017). The mechanisms and functions of synaptic facilitation. Neuron 94, 447–464.

Jones, B.W., Deem, J., Younts, T.J., Weisenhaus, M., Sanford, C.A., Slack, M.C., Chin, J., Nachmanson, D., McKennon, A., Castillo, P.E., and McKnight, G.S. (2016). Targeted deletion of AKAP7 in dentate granule cells impairs spatial discrimination. eLife 5, e20695.

Josselyn, S.A., and Tonegawa, S. (2020). Memory engrams: Recalling the past and imagining the future. Science 367, eaaw4325.

Klausberger, T., Magill, P.J., Márton, L.F., Roberts, J.D., Cobden, P.M., Buzsáki, G., and Somogyi, P. (2003). Brain-state- and cell-type-specific firing of hippocampal interneurons in vivo. Nature 421, 844–848.

Korogod, N., Lou, X., and Schneggenburger, R. (2005). Presynaptic Ca^{2+} requirements and developmental regulation of posttetanic potentiation at the calyx of Held. J. Neurosci. 25, 5127–5137.

Kowalski, J., Gan, J., Jonas, P., and Pernía-Andrade, A.J. (2016). Intrinsic membrane properties determine hippocampal differential firing pattern in vivo in anesthetized rats. Hippocampus 26, 668–682.

Langdon, R.B., Johnson, J.W., and Barrionuevo, G. (1995). Posttetanic potentiation and presynaptically induced long-term potentiation at the mossy fiber synapse in rat hippocampus. J. Neurobiol. 26, 370–385.

Lashley, K.S. (1950). In search of the engram. In Symposia of the Society of Experimental Biology, No. 4: Physiological Mechanisms in Animal Behavior, J.F. Danielli and R. Brown, eds. (Cambridge University Press), pp. 454–482.

Lee, J.S., Kim, M.H., Ho, W.K., and Lee, S.H. (2008). Presynaptic release probability and readily releasable pool size are regulated by two independent mechanisms during posttetanic potentiation at the calyx of Held synapse. J. Neurosci. 28, 7945–7953.

Lee, J.S., Ho, W.K., and Lee, S.H. (2010). Post-tetanic increase in the fast-releasing synaptic vesicle pool at the expense of the slowly releasing pool. J. Gen. Physiol. 136, 259–272.

Lee, J.S., Ho, W.K., Neher, E., and Lee, S.H. (2013). Superpriming of synaptic vesicles after their recruitment to the readily releasable pool. Proc. Natl. Acad. Sci. USA 110, 15079–15084.

Liu, X., Ramirez, S., Pang, P.T., Puryear, C.B., Govindarajan, A., Deisseroth, K., and Tonegawa, S. (2012). Optogenetic stimulation of a hippocampal engram activates fear memory recall. Nature 484, 381–385.

Midorikawa, M., and Sakaba, T. (2017). Kinetics of releasable synaptic vesicles and their plastic changes at hippocampal mossy fiber synapses. Neuron 96, 1033–1040.e3.

Miki, T., Nakamura, Y., Malagon, G., Neher, E., and Marty, A. (2018). Two-component latency distributions indicate two-step vesicular release at simple glutamatergic synapses. Nat. Commun. 9, 3943.

Mistry, R., Dennis, S., Frerking, M., and Mellor, J.R. (2011). Dentate gyrus granule cell firing patterns can induce mossy fiber long-term potentiation in vitro. Hippocampus 21, 1157–1168.

Mongillo, G., Barak, O., and Tsodyks, M. (2008). Synaptic theory of working memory. Science 319, 1543–1546.

Murthy, V.N., and Stevens, C.F. (1999). Reversal of synaptic vesicle docking at central synapses. Nat. Neurosci. 2, 503–507.

Neher, E. (2015). Merits and limitations of vesicle pool models in view of heterogeneous populations of synaptic vesicles. Neuron 87, 1131–1142.

Neunuebel, J.P., and Knierim, J.J. (2012). Spatial firing correlates of physiologically distinct cell types of the rat dentate gyrus. J. Neurosci. 32, 3848–3858.

Nicoll, R.A., and Schmitz, D. (2005). Synaptic plasticity at hippocampal mossy fibre synapses. Nat. Rev. Neurosci. 6, 863–876.

Patzke, C., Brockmann, M.M., Dai, J., Gan, K.J., Grauel, M.K., Fenske, P., Liu, Y., Acuna, C., Rosenmund, C., and Südhof, T.C. (2019). Neuromodulator signaling bidirectionally controls vesicle numbers in human synapses. Cell 179, 498–513.e22.

Pernía-Andrade, A.J., and Jonas, P. (2014). Theta-gamma-modulated synaptic currents in hippocampal granule cells in vivo define a mechanism for network oscillations. Neuron 81, 140–152.

Pernía-Andrade, A.J., Goswami, S.P., Stickler, Y., Fröbe, U., Schlögl, A., and Jonas, P. (2012). A deconvolution-based method with high sensitivity and temporal resolution for detection of spontaneous synaptic currents in vitro and in vivo. Biophys. J. 103, 1429–1439.

Pilz, G.A., Carta, S., Stäuble, A., Ayaz, A., Jessberger, S., and Helmchen, F. (2016). Functional imaging of dentate granule cells in the adult mouse hippocampus. J. Neurosci. 36, 7407–7414.

Rancz, E.A., Ishikawa, T., Duguid, I., Chadderton, P., Mahon, S., and Häusser, M. (2007). High-fidelity transmission of sensory information by single cerebellar mossy fibre boutons. Nature 450, 1245–1248.

Regehr, W.G., Delaney, K.R., and Tank, D.W. (1994). The role of presynaptic calcium in short-term enhancement at the hippocampal mossy fiber synapse. J. Neurosci. 14, 523–537.

Rollenhagen, A., Sätzler, K., Rodríguez, E.P., Jonas, P., Frotscher, M., and Lübke, J.H.R. (2007). Structural determinants of transmission at large hippocampal mossy fiber synapses. J. Neurosci. 27, 10434–10444.

Royer, S., Zemelman, B.V., Losonczy, A., Kim, J., Chance, F., Magee, J.C., and Buzsáki, G. (2012). Control of timing, rate and bursts of hippocampal place cells by dendritic and somatic inhibition. Nat. Neurosci. 15, 769–775.

Sakaba, T., and Neher, E. (2003). Involvement of actin polymerization in vesicle recruitment at the calyx of Held synapse. J. Neurosci. 23, 837–846.

Salin, P.A., Scanziani, M., Malenka, R.C., and Nicoll, R.A. (1996). Distinct short-term plasticity at two excitatory synapses in the hippocampus. Proc. Natl. Acad. Sci. USA 93, 13304–13309.

Schneggenburger, R., Meyer, A.C., and Neher, E. (1999). Released fraction and total size of a pool of immediately available transmitter quanta at a calyx synapse. Neuron 23, 399–409.

Silver, R.A. (2010). Neuronal arithmetic. Nat. Rev. Neurosci. 11, 474–489.

Squire, L.R., and Zola-Morgan, S. (1991). The medial temporal lobe memory system. Science 253, 1380–1386.

Taschenberger, H., Woehler, A., and Neher, E. (2016). Superpriming of synaptic vesicles as a common basis for intersynapse variability and modulation of synaptic strength. Proc. Natl. Acad. Sci. USA 113, E4548–E4557.

Thanawala, M.S., and Regehr, W.G. (2013). Presynaptic calcium influx controls neurotransmitter release in part by regulating the effective size of the readily releasable pool. J. Neurosci. 33, 4625–4633.

Toth, K., Suares, G., Lawrence, J.J., Philips-Tansey, E., and McBain, C.J. (2000). Differential mechanisms of transmission at three types of mossy fiber synapse. J. Neurosci. 20, 8279–8289.

Vyleta, N.P., and Jonas, P. (2014). Loose coupling between Ca^{2+} channels and release sensors at a plastic hippocampal synapse. Science 343, 665–670.

Vyleta, N.P., Borges-Merjane, C., and Jonas, P. (2016). Plasticity-dependent, full detonation at hippocampal mossy fiber-CA3 pyramidal neuron synapses. eLife 5, e17977.

Watanabe, S., Liu, Q., Davis, M.W., Hollopeter, G., Thomas, N., Jorgensen, N.B., and Jorgensen, E.M. (2013a). Ultrafast endocytosis at Caenorhabditis elegans neuromuscular junctions. eLife *2*, e00723.

Watanabe, S., Rost, B.R., Camacho-Pérez, M., Davis, M.W., Söhl-Kielczynski, B., Rosenmund, C., and Jorgensen, E.M. (2013b). Ultrafast endocytosis at mouse hippocampal synapses. Nature *504*, 242–247.

Weisskopf, M.G., Castillo, P.E., Zalutsky, R.A., and Nicoll, R.A. (1994). Mediation of hippocampal mossy fiber long-term potentiation by cyclic AMP. Science *265*, 1878–1882.

Wiebe, S.P., and Stäubli, U.V. (1999). Dynamic filtering of recognition memory codes in the hippocampus. J. Neurosci. *19*, 10562–10574.

Zenke, F., Agnes, E.J., and Gerstner, W. (2015). Diverse synaptic plasticity mechanisms orchestrated to form and retrieve memories in spiking neural networks. Nat. Commun. *6*, 6922.

Zucker, R.S., and Regehr, W.G. (2002). Short-term synaptic plasticity. Annu. Rev. Physiol. *64*, 355–405.

STAR★METHODS

KEY RESOURCES TABLE

REAGENT or RESOURCE	SOURCE	IDENTIFIER
Chemicals, Peptides, and Recombinant Proteins		
Tamoxifen	Sigma-Aldrich	Cat # T5648-1G
Corn Oil	Sigma-Aldrich	Cat # C8267-500 ml
NaCl	VWR (Merck)	Cat # 1.06404.1000
Sucrose	Sigma-Aldrich	Cat # 16104
NaHCO$_3$	VWR (Merck)	Cat # 1.06329.1000
D-glucose	VWR (Merck)	Cat # 1.08342.1000
KCl	VWR (Merck)	Cat # 26764.232
Na$_2$HPO$_4$	VWR (Merck)	Cat#1.06580.0500
NaH$_2$PO$_4$	VWR (Merck)	Cat # 1.06346.0500
CaCl$_2$	VWR (Merck)	Cat # 1.02382.0250
MgCl$_2$	Honeywell	Cat # M9272-1KG
HEPES	Sigma-Aldrich	Cat # M3375-100G
EGTA	Sigma-Aldrich	Cat # EO396-100G
Na$_2$ATP	Sigma-Aldrich	Cat # A3377-100G
Polyvinylpyrrolidone (PVP)	Sigma-Aldrich	Cat # PVP10-100G
Sodium azide	Sigma-Aldrich	Cat # S8032-25G
Osmium tetroxide	Science services (EMS)	Cat # 19130
Durcupan ACM Resin Single component A	Sigma-Aldrich	Cat # 44611-100 ml
Durcupan ACM Resin Single component B	Sigma-Aldrich	Cat # 44612-100 ml
Durcupan ACM Resin Single component C	Sigma-Aldrich	Cat # 44613-100 ml
Durcupan ACM Resin Single component D	Sigma-Aldrich	Cat # 44614-100 ml
Uranyl acetate 2 H$_2$O	Serva	Cat # 77870.02
Lead (II) nitrate	Sigma-Aldrich	Cat # 228621-100G
Acetone, HPLC grade	ChemLab	Cat # CL00.0172.2500
Ketamine	Intervet	Z.Nr. 8-00335 100 mg/ml
Xylazine	Graeub	Z.Nr. 8-00178 20 mg/ml
Lidocaine	Sigma	L-1026-1VL
Dexpanthenol ointment	Bayer	Cat # PZN 0829388
Cyanoacrylate superglue	Uhu	Cat #45570 3 g
Metacam	Boehringer	2 mg/ml
Silicone elastomer	Kwik-cast, World Precision Instruments	N/A
Potassium D-Gluconate	Sigma-Aldrich	Cat # G4500-100 g
NaGTP	Sigma-Aldrich	Cat # G8877-250 mg
Biocytin	Molecular probes	Cat # B1592
Paraformaldehyde	TAAB	Cat # FO 17/1
Glutaraldehyde	Carl Roth	Cat # 4157.1
Saturated picric acid solution	Sigma-Aldrich	Cat # P6744-1GA
Triton X-100	Sigma-Aldrich	Cat # X100-100ml
Avidin-biotinylated horseradish peroxidase complex	ABC, Vector Laboratories	Cat # PK6100
3,3′-Diaminobenzidine tetrahydrochloride	Sigma-Aldrich	Cat # D5637-5 g
Cobalt	Sigma-Aldrich	Cat # C8661-25 g
Nickel (II) chloride hexahydrate	Sigma-Aldrich	Cat # 223387-25 g

Continued

REAGENT or RESOURCE	SOURCE	IDENTIFIER
Mowiol 4-88	Carl Roth	Cat # 713.2
Cytochalasin D	Tocris	Cat # 1233
Latrunculin B	Tocris	Cat # 3974/1
H-89 dihydrochloride	Tocris	Cat # 2910/10
Tetrodotoxin citrate	Tocris	Cat # 1069/1
Tetraethylammonium chloride	Sigma-Aldrich	Cat # T2265
Cesium chloride	Sigma-Aldrich	Cat # C3011-25 g
H_2O_2	Sigma-Aldrich	Cat # 95321-100 ml
Tris(hydroxymethyl)aminomethane	Sigma-Aldrich	Cat #252859-100 g
Glycerol	Sigma-Aldrich	Cat # G9012-500 ml
HCl	Merck	1.09057.1000
Experimental Models: Organisms/Strains		
Prox1-CreER^{T2} mouse line	Bazigou et al., 2011	PMID: 21765212
C57BL6/J wild-type mice	Charles River Germany (from The Jackson Laboratory)	RRID:IMSR_JAX:000664
B6;129S-Gt(ROSA)26Sor$^{tm32(CAG-COPA*H134R/EYFP)Hze}$/J mouse line	The Jackson Laboratory	RRID:IMSR_JAX:012569
Wistar Rats	Preclinical facility, IST Austria Janvier Labs	RRID:RGD_13508588
Software and Algorithms		
Multiclamp (version 1.3.0.05)	Axon Instruments/Molecular Devices	https://www.moleculardevices.com/
Igor Pro (version 6.3.4.1)	WaveMetrics	https://www.wavemetrics.com/
Radius Software	EMSIS	https://www.emsis.eu/products/software/radius/
Stimfit (version 0.14.14)	Guzman et al., 2014	PMID: 24600389
AxoGraph (version 1.7.2)	AxoGraph	https://axograph.com/
Fiji (ImageJ version 2.0.0-rc-69/1.52n)	NIH, Open source	https://fiji.sc/
Graphpad Prism (version 8)	Graphpad	https://www.graphpad.com/
Adobe Illustrator (version 23.0.4)	Adobe	https://www.adobe.com/products/illustrator.html
HEKA Patchmaster acquisition software (2x90.1)	HEKA	https://www.heka.com/
Coreldraw X8	Coreldraw	https://www.coreldraw.com/en/
MATLAB 2016, 2018	MathWorks	https://www.mathworks.com/
Coreldraw 2018	Coreldraw	https://www.coreldraw.com/en
Origin 2018	OriginLab	https://www.originlab.com/
Python 2.7	Python	https://www.python.org/
Mathematica 12.0.0.0	Wolfram Research	https://www.wolfram.com/mathematica/
Other		
Borosilicate glass (2 mm outside/ 1 mm inside)	Hilgenberg	Cat# 1907542

RESOURCE AVAILABILITY

Lead Contact
Further information and requests for resources should be directed to and will be fulfilled by the Lead Contact, Peter Jonas (peter.jonas@ist.ac.at).

Materials Availability
This study did not generate new unique reagents.

Data and Code Availability

Original data, analysis programs, and computer code were stored in the scientific repositories of the Institute of Science and Technology Austria and are available upon reasonable request.

EXPERIMENTAL MODEL AND SUBJECT DETAILS

Animal experiments

Whole-cell patch-clamp recordings *in vivo* were performed in 35- to 63-day-old C57BL/6 mice (RRID:IMSR_JAX:000664). Paired pre- and postsynaptic recordings *in vitro* were carried out on 19- to 23-day-old Wistar rats (RRID:RGD_13508588; weight: 55–65 g). Functional electron microcopy ("flash and freeze") experiments were preformed using Prox1-creER^{T2} (PMID: 21765212; Bazigou et al., 2011) x Ai32 B6;129S-Gt(ROSA)26Sortm32(CAG-COPA*H124R/EYFP)Hze/J (Jackson Laboratory; RRID:IMSR_JAX:012569) crossed mice (Borges-Merjane et al., 2020). Animals were housed under a reversed light cycle (dark: 7:00 am – 7:00 pm, light: 7:00 pm – 7:00 am). For experiments, both male and female animals were used. Experiments were carried out in strict accordance with institutional, national, and European guidelines for animal experimentation, and approved by the Bundesministerium für Wissenschaft, Forschung und Wirtschaft of Austria (A. Haslinger, Vienna; BMWFW-66.018/0007-WF/II/3b/2014, BMWFW-66.018/010-WF/V/36/2015, and BMWFW-66.018/0008-V/3b/2018).

METHOD DETAILS

In vivo recordings from identified dentate gyrus GCs

To characterize AP frequency, timing, and pattern in morphologically identified GCs, we analyzed a previously acquired dataset from 43 active neurons (X.Z., A. Schlögl, and P.J., unpublished data). Whole-cell patch-clamp recordings *in vivo* were performed in 35- to 63-day-old C57BL/6 mice of either sex (RRID:IMSR_JAX:000664). Animals were head-fixed, but able to run on a linear belt (Royer et al., 2012; Bittner et al., 2015). Head-bar implantation and craniotomy were performed under anesthesia by intraperitoneal injection of 80 mg kg^{-1} ketamine (Intervet) and 8 mg kg^{-1} xylazine (Graeub), followed by local anesthesia with lidocaine. A custom-made steel head-bar was attached to the skull using superglue and dental cement. After 1 week of recovery, animals were mildly water-restricted for 1 week (2 mL per day), and trained to run on the linear belt for 7–10 days. Water rewards were given when the animal ran over a distance of 180 cm.

The day before recording, two small craniotomies (~0.5 mm in diameter), one for the patch electrode and one for the LFP electrode, were drilled at the following coordinates: approximately −2.0 mm and −2.5 mm anterio-posterior (whole-cell recording and LFP, respectively; measured from bregma), and ~1.2 mm medio-lateral (measured from midline). The dura was left intact, and craniotomies were covered with silicone elastomer (Kwik-Cast, World Precision Instruments). Pipettes were fabricated from borosilicate glass capillaries (1.75 mm outer diameter, 1.25 mm inner diameter). Long-taper whole-cell patch electrodes (9–12 MΩ) were filled with a solution containing: 130 mM K-gluconate, 2 mM KCl, 2 mM MgCl$_2$, 2 mM Na$_2$ATP, 0.3 mM NaGTP, 10 mM HEPES, 18 mM sucrose, 10 or 0.1 mM EGTA, and 0.3% biocytin (pH adjusted to 7.28 with KOH). LFP electrodes (4–6 MΩ) were filled with artificial cerebrospinal fluid (ACSF) solution. Whole-cell patch electrodes were advanced through the cortex with 500–600 mbar of pressure to prevent the electrode tip from clogging. After passing the hippocampal CA1 subfield, the pressure was reduced to 20 mbar. After a blind whole-cell recording was obtained, series resistance was calculated by applying a test pulse (+50 mV and −10 mV) under voltage-clamp conditions. Recordings were immediately discarded if series resistance exceeded 80 MΩ. Bridge balance and pipette capacitance compensation was enabled throughout the recording.

Recordings were performed in the current-clamp configuration without current injection using a HEKA EPC double amplifier. Signals were low-pass filtered at 10 kHz (Bessel) and sampled at 25 kHz with Heka Patchmaster acquisition software. At the end of each recording, the patch pipettes were slowly withdrawn to form an outside-out patch, verifying the integrity of the seal.

APs were detected when the derivative of membrane potential signal was > 50 V s^{-1}. ISI distributions were fit with two or three Gaussian components using a maximum-likelihood procedure. To assess statistical significance, data were analyzed by bootstrap procedures (Efron and Tibshirani, 1998). Original datasets were duplicated 1000 times, randomly permuted, and cut into blocks of original size. Log-likelihood ratios of original data were compared against values of bootstrap replications. The LFP signal was detrended and down-sampled to 2.5 kHz. Then, the LFP signal was band-pass filtered in the delta (2-4 Hz), theta (5–10 Hz), and gamma range (30–80 Hz), respectively. Hilbert transformation was applied to each signal to extract information about power and phase. Theta and delta power were smoothed using a 2 s sliding window. Epochs were classified as theta if the mean theta-delta power ratio within 2-s time windows was > 4 (Klausberger et al., 2003).

Brain slice preparation

Transverse hippocampal slices (350–400 μm thick) were prepared from 19- to 23-day-old Wistar rats of either sex (RRID:RGD_13508588; weight: 55–65 g) according to previously established protocols (Bischofberger et al., 2006). This age and weight range was chosen because morphological properties of mossy fiber synapses were largely mature, while paired recording experiments became increasingly difficult at later stages. Rats were kept under a heating lamp for 1 hour prior to dissection. Animals were lightly anesthetized by isoflurane and killed by rapid decapitation, in accordance with institutional, national, and European

guidelines. Slices were cut from the right hemisphere in ice-cold, sucrose-containing extracellular solution using a vibratome (VT1200, Leica Microsystems), incubated in a maintenance chamber at ∼33°C for 45 min for recovery, and subsequently stored at room temperature. High-sucrose ACSF used for cutting contained 64 mM NaCl, 25 mM NaHCO$_3$, 2.5 mM KCl, 1.25 mM NaH$_2$PO$_4$, 10 mM glucose, 120 mM sucrose, 0.5 mM CaCl$_2$, and 7 mM MgCl$_2$. High-sucrose ACSF used for storage contained 87 mM NaCl, 25 mM NaHCO$_3$, 2.5 mM KCl, 1.25 mM NaH$_2$PO$_4$, 10 mM glucose, 75 mM sucrose, 0.5 mM CaCl$_2$, and 7 mM MgCl$_2$, equilibrated with 95% O$_2$ and 5% CO$_2$, ∼325 mOsm. Experiments were performed at room temperature (24.1 ± 0.2°C; range: 21–26°C), and, in a subset of measurements, at near-physiological temperature (∼32°C; range: 29.4–34.0°C; Figure S1). Before onset of the experiment, slices were placed in the recording chamber (∼1 mL volume) and superfused with ACSF (125 mM NaCl, 25 mM NaHCO$_3$, 2.5 mM KCl, 1.25 mM NaH$_2$PO$_4$, 2 mM CaCl$_2$, and 1 mM MgCl$_2$) for at least 15 minutes before recording.

Presynaptic cell-attached and whole-bouton recording

Subcellular patch-clamp recordings from mossy fiber boutons and simultaneous recordings from pyramidal neurons in the CA3b,c region of the hippocampus were performed under visual control (Bischofberger et al., 2006; Vyleta and Jonas, 2014). Presynaptic recording pipettes were fabricated from borosilicate glass capillaries (2.0 mm outer diameter, 1.0 mm inner diameter), and had open-tip resistances of 10–20 MΩ. For tight-seal, bouton-attached stimulation under voltage-clamp conditions, the presynaptic pipette contained a K$^+$-based intracellular solution (130 mM K-gluconate, 2 mM KCl, 2 mM MgCl$_2$, 2 mM Na$_2$ATP, 10 mM HEPES, 10 mM EGTA, pH adjusted to 7.3 with KOH, 297–300 mOsm), allowing us to measure bouton properties in both cell-attached and subsequent whole-bouton configuration. The presynaptic holding potential was set at –70 mV to minimize the holding current (less than −10 pA in all pairs; Alcami et al., 2012). APs in mossy fiber boutons were evoked by brief voltage pulses (amplitude 800 mV, duration 0.1 ms). In the absence of stimulation, action currents were not observed, indicating that bouton-attached stimulation permitted the reliable and precise control of activity in a single presynaptic input. Boutons had diameters of ∼2–5 μm, in agreement with the previously reported range of diameters of mossy fiber boutons in light and electron microscopy studies (Chicurel and Harris, 1992; Acsády et al., 1998; Rollenhagen et al., 2007; Borges-Merjane et al., 2020). Stimuli (10 stimuli at 50 Hz) were delivered once every 20 s (i.e., at 0.05 Hz). For mEPSC recordings (Figure 4), a cesium-based internal solution (145 mM CsCl, 2 mM MgCl$_2$, 2 mM Na$_2$ATP, 0.3 mM Na$_2$GTP, 5 mM Na$_2$phosphocreatine, 10 mM EGTA, and 10 mM HEPES, pH was adjusted to 7.3 with CsOH) was used. The presynaptic terminal was held in the whole-cell voltage-clamp configuration, and mossy fiber mEPSCs were evoked by depolarizing the terminal for 4 s to −10 mV.

Postsynaptic whole-cell somatic recording

Postsynaptic recording pipettes were fabricated from borosilicate glass tubing (2.0 mm outer diameter, 1.0 mm inner diameter), and had open-tip resistances of 3–7 MΩ. They contained an internal solution with 130 mM K-gluconate, 20 mM KCl, 2 mM MgCl$_2$, 2 mM Na$_2$ATP, 10 mM HEPES, and 10 mM EGTA (pH adjusted to 7.28 with KOH, 312–315 mOsm). Voltage-clamp recordings were performed at –70 mV, and only recordings with < 200 pA injection of hyperpolarizing current were included in the analyses. Postsynaptic series resistance was in the range 4.5–18.3 MΩ, mean ± SEM 7.1 ± 0.2 MΩ; median 6.2 MΩ (106 mossy fiber terminal–CA3 pyramidal neuron recordings). Series resistance was uncompensated, but carefully monitored with a test pulse following each data acquisition sweep. Only recordings with stable series resistance were included in the analysis. Paired recordings with tight-seal, bouton-attached stimulation were stable for up to 30 min. For mEPSC experiments, 1 μM TTX and 10 mM tetraethylammonium (TEA) were added to the bath solution. In subsets of recordings, 10 μM of the PKA blocker H-89 (10 mM stock solution in DMSO) or 20 or 10 μM, respectively, of the actin polymerization inhibitors latrunculin B and cytochalasin D (10 mM stock solution in DMSO) were added to the bath solution (Figure 6). In another subset (Figure S3), 1 mM of the low-affinity competitive AMPA receptor antagonist kynurenic acid was added to the bath to minimize saturation or desensitization of postsynaptic receptors (Habets and Borst, 2005; Geiger et al., 1995). Chemicals were from Sigma-Aldrich, Merck, or Tocris.

PTP induction protocols

Data were acquired with a Multiclamp 700A amplifier, low-pass filtered at 10 kHz, and digitized at 100 kHz using a CED power1401 mkII interface (Cambridge Electronic Design, Cambridge, UK). Pulse generation and data acquisition were performed using FPulse version 3.3.3 (U. Fröbe, Freiburg, Germany). To induce PTP, an HFS$_{100APs}$ stimulation paradigm (100 stimuli at 100 Hz in tight-seal cell-attached mode) was applied to the mossy fiber terminal. In experiments in which the PTP induction threshold was measured (Figures 2B–2G), HFS$_{3APs}$, HFS$_{9APs}$, HFS$_{18APs}$, HFS$_{36APs}$, and HFS$_{72APs}$ paradigms (all at 100 Hz) were delivered to the presynaptic terminal. In experiments with physiological activity patterns (Figures 2H and 2I; Figures S1G–S1I), SBs with 10 and 24 APs taken from *in vivo* recordings were applied. The postsynaptic CA3 pyramidal neuron was recorded under voltage-clamp conditions throughout. In experiments in which mEPSCs were recorded after PTP induction (Figure 4), PTP was induced by HFS$_{100APs}$ in the presynaptic cell-attached configuration, followed by rapid bath application of 1 μM TTX + 10 mM TEA, transition into the presynaptic whole-cell configuration, and subthreshold terminal depolarization to −10 mV. The first depolarizing pulse was applied ∼20 s after HFS.

Thin-slice preparation for functional electron microscopy

"Flash and freeze" experiments were performed as previously described (Watanabe et al., 2013a, 2013b; Borges-Merjane et al., 2020). To enable optogenetic GC stimulation, Prox1-CreER^{T2} (PMID: 21765212; Bazigou et al., 2011) x Ai32 B6;129S-Gt(ROSA) 26Sortm32(CAG-COPA*H124R/EYFP)Hze/J (Jackson Laboratory; RRID:IMSR_JAX:012569) crossed mice were used. For maximum expression of channelrhodopsin in GCs, each mouse received two intraperitoneal (IP) injections of tamoxifen in corn oil (Sigma; 100 mg × kg^{-1} of mouse body weight) given 2–3 days apart. This procedure resulted in maximal labeling of GCs (Borges-Merjane et al., 2020). Mice were used for experiments after a minimum of 7–10 days after injections. Horizontal hippocampal slices were sectioned at 200 μm thickness for high-pressure freezing and 300 μm thickness for electrophysiology control experiments (Figure S6B) using a vibratome (VT1200S, Leica Microsystems) in ice-cold high-sucrose ACSF. Slices were recovered in high-sucrose ACSF at 35°C for 30–45 min for recovery, transferred to ACSF solution identical to recording solution, and kept at room temperature (~23°C) during storage for up to 4 hours. Finally, slices were heated to physiological temperature (37°C) for 5–10 minutes directly before freezing.

High-pressure freezing

High-pressure freezing was performed with a Leica EM ICE high-pressure freezing apparatus equipped with a blue LED light stimulation module (460 nm wavelength; light intensity at specimen 5.5–8.0 mW mm^{-2}). After slicing and recovery, slices were mounted in a sapphire-metal ring sandwich (Figure 5A; Borges-Merjane et al., 2020). For mounting, first a bottom sapphire disk (diameter 6 mm, thickness 120 μm; Leica or Wohlwend, Sennwald, Switzerland) was placed on the middle plate of a clear cartridge. Then the spacer ring (outer diameter 6 mm, inner diameter 5 mm; thickness 200 μm) was put with a drop of ACSF containing 15% of the cryoprotectant polyvinylpyrrolidone over the ring to adhere it to the sapphire. Next, the tissue sample was transferred. Finally, the second sapphire disk was put on top to close the sandwich. Slices were transferred carefully but quickly, using a paintbrush number 4 covered with solution. During the entire mounting procedure, the specimen assembly table and the freezing chamber of the Leica EM ICE were kept at 37°C. To keep track of the light-stimulated side, slices from left and right hemispheres were frozen separately.

Freeze substitution, embedding, and electron microscopy

Freeze substitution was performed using an AFS1 or AFS2 freeze substitution system (Leica) equipped with an agitation module, as previously described (Borges-Merjane et al., 2020). For the first day of freeze substitution, the high-pressure frozen samples were transferred from liquid nitrogen to vials with 0.1% tannic acid in acetone, frozen in liquid nitrogen. Vials were then transferred to the AFS1 or AFS2 systems kept at −90°C, and shaken overnight for 22–24 hours. On the second day, samples were washed, while kept inside the freeze-substitution machines, with acetone chilled to −90°C 3–4 times for 10 minutes each. Next, the contrasting cocktail with 2% osmium and 0.2% uranyl acetate in acetone, also first chilled to −90°C, was added to each vial and shaken overnight. Samples were kept at −90°C for 7–10 hours.

Next the temperature was raised to −60°C within 2 hours (15°C/hour), kept at −60°C for 3 hours, raised to −30°C within 4 hours (7.5°C/hour), kept at −30°C for 3 hours; and finally raised to 0°C within 3 hours (10°C/hour). Samples were then kept at 0°C only for ~10 min. Once the substitution protocol was completed, vials were transferred to ice for washes with acetone (3 × 10 min). They were then transferred to glass dishes with acetone at room temperature for inspection, to ensure that slices were intact and sandwiches properly opened and infiltrated. Samples were then washed with propylene oxide (2 × 10 min), and infiltrated with Durcupan resin at 2:1, 1:1, and 1:2 propylene oxide/Durcupan resin mix (1 h at room temperature), shaking. They were then left in pure resin overnight at room temperature, and embedded in BEEM capsules (Electron Microscopy Sciences, Hatfield, PA, USA). Capsules were polymerized overnight at 100°C. Slices were carefully embedded with the light-stimulated side facing down, for ultramicrotomy.

Embedded capsules were trimmed with glass knives and ultrathin sections were taken in a Leica EM UC7 Ultramicrotome with Diatome Histo (for 70-nm sections) diamond knives. Sections were kept in slot grids with formvar for TEM imaging. Post-staining was done with 10 minutes in 4% uranyl acetate followed by 2 minutes in lead citrate. Images of ultrathin sections were taken with a transmission electron microscope (FEI Tecnai 10, 80 kV accelerating voltage) with an OSIS Megaview III camera and Radius acquisition software.

QUANTIFICATION AND STATISTICAL ANALYSIS

Electrophysiology data analysis

Data were analyzed with Stimfit version 0.14.14 (Guzman et al., 2014) and Igor Pro version 6.3.4.1 (Wavemetrics). During trains of 10 or 100 stimuli, the peak amplitude of each EPSC was measured directly from the preceding baseline. PTP decay time course was fit with a mono-exponential function plus an offset. For analysis of PTP magnitude and time course, only pairs with stationary control conditions, as indicated by lack of significant correlation in the baseline epoch, were used. PTP was computed as Max[EPSC$_1$ after HFS] / Mean[EPSC$_1$ in control], where Max is the maximal EPSC$_1$ at 20, 40, or 60 s after HFS, and Mean is the mean of 5 EPSC$_1$ control values before HFS. The paired-pulse ratio EPSC$_2$ / EPSC$_1$ was computed from an average trace (from 5 individual traces) before HFS and a single trace after HFS.

For analysis of RRP size, P$_r$, and refilling rate, cumulative EPSC peak amplitude was plotted against time for 10 and 100 stimuli. For analysis with the Schneggenburger-Meyer-Neher method (SMN; Schneggenburger et al., 1999), the last 3–5 and 30–50 data points,

respectively, were fit by linear regression. Traces in which the extent of depression (average of the last three/thirty EPSCs compared with peak EPSC) was < 50% (Neher, 2015) were excluded from the analysis (18% of traces total). The size of the RRP was determined as the intersection of the regression line with the ordinate, P_r was measured as the ratio of the first EPSC amplitude over pool size, and refilling rate was obtained from the slope of the line. For analysis with the Thanawala-Regehr method (TR; Thanawala and Regehr, 2013), the EPSC amplitude data points were fit with a product of an exponential facilitation and an exponential depression function. The depression component g(x) was extracted, normalized, and integrated to G(x). Finally, the cumulative EPSC peak amplitude data were fit by the linear combination a * G(x) + b. The size of the RRP was determined as the intersection of the fit curve with the ordinate, and P_r was measured as the ratio of the first EPSC amplitude over pool size. For both methods (Schneggenburger et al., 1999; Thanawala and Regehr, 2013), the RRP estimates represent "pool decrement" rather than absolute pool size; the true pool size will be larger than the estimate (Neher, 2015). Using the correction previously suggested for a single homogeneous pool (Neher, 2015), and assuming $y_{10} / y_0 = 0.5$, and $p_{10} / p_0 = 6$ (Vyleta and Jonas, 2014, their Figure S5B), the correction factor pool size / pool decrement would be estimated as 1.09. 50-Hz trains of ten stimuli applied every 20 s evoked stationary responses, suggesting that they were below the PTP induction threshold (stationary test based on linear regression analysis of baseline periods without stimulation; p > 0.2; 10 pairs).

For detection of mEPSCs, a machine-learning based detection algorithm was used (MOD; X.Z., A. Schlögl, D.V., and P.J., unpublished data). Subsets of the data were manually scored, and the filter coefficients of an optimal Wiener filter were computed so that they reproduced the manual scoring trace as closely as possible. The detection threshold was set to a value that maximized Cohen's κ coefficient. In the current dataset, the area under the curve (AUC) in a plot of true positive against false positive rate was 0.960 ± 0.005, demonstrating reliable and efficient detection of synaptic events (Pernía-Andrade et al., 2012).

Electron micrograph analysis

Electron micrographs were analyzed with Fiji open source software. Hippocampal mossy fiber terminals in *stratum lucidum* of CA3b and CA3c subregions were unequivocally identified based on large size, multiple active zones, synaptic contacts on thorny excrescences of CA3 pyramidal cells, *puncta adherentia* on dendritic shafts, high density of small clear vesicles, and presence of large dense core vesicles (Borges-Merjane et al., 2020; Chicurel and Harris, 1992; Rollenhagen et al., 2007). Active zones were defined as the presynaptic membrane regions directly opposed to postsynaptic densities (asymmetric contacts), accumulation of synaptic vesicles, and characteristic widening of the synaptic cleft (Chicurel and Harris, 1992; Rollenhagen et al., 2007). Vesicles that were less than 5 nm from the active zone membrane were considered docked. For quantification of number of docked vesicles per profile and vesicle diameters, counts were normalized to 100 nm of active zone length. A minimum of 154 active zones profiles were analyzed per animal, and at least three animals were examined per condition. All vesicle counting and image analysis was done with the experimenter blind to the experimental condition. Depletion data were taken from a previously published Neuroresource paper; experiments for the two datasets were performed in an interleaved manner (Borges-Merjane et al., 2020).

Modeling of pool dynamics

EPSC amplitudes during trains were modeled using a model with three pools (pool$_0$, pool$_1$, and pool$_2$, intended to represent docked, primed, and superprimed synaptic vesicles), filled from an upstream pool of infinite size via a refilling process. The model was described by the following differential equations

$$\frac{dp_0(t)}{dt} = r_{10}\, p_1(t) - r_{01}\, p_0(t) + r(t), \tag{Eq. 1}$$

$$\frac{dp_1(t)}{dt} = r_{01}\, p_0(t) - r_{10}\, p_1(t) + r_{21}\, p_2(t) - r_{12}\, p_1(t) - f(t)P_{r1}\, p_1(t), \tag{Eq. 2}$$

$$\frac{dp_2(t)}{dt} = r_{12}\, p_1(t) - r_{21}\, p_2(t) - f(t)P_{r2}\, p_2(t), \text{ and} \tag{Eq. 3}$$

$$\frac{ds(t)}{dt} = \theta(t) - s(t)\Big/ \tau_s, \tag{Eq. 4}$$

where p_i represents the number of vesicles in pool i (i = 0, 1, 2), r_{ij} is the transition rate between pool i and pool j (i, j = 0, 1, 2, i $\neq$ j), P_{r1} and P_{r2} are the release probabilities of primed and superprimed vesicles ($P_{r2} > P_{r1}$), r is the total refilling rate (comprising refilling from an infinite reserve pool and multiple forms of endocytosis from the plasma membrane; Chanaday and Kavalali, 2018), f is a facilitation factor (constrained according to $P_r \times f \leq 1$), and $\theta(t)$ is a function representing a sequence of pulses of 1 ms duration and unitary amplitude. r(t) was computed as $r_1 \times s(t)^{ms} / (s(t)^{ms} + s_{half}^{ms}) + r_0$, where m_s is a power coefficient of refilling, and r_0 and r_1 are basal and activity-dependent refilling rate, respectively. r_0 was set to 0 before and after stimulation periods. Similarly, f(t) was computed as

$(f_{max} - 1) \times s(t)^{mf} / (s(t)^{mf} + s_{half}^{mf}) + 1$, where m_f is the power coefficient of facilitation. Quantal size was assumed as 50 pA. Equations were solved using NDSolve of Mathematica 12.0.

To obtain the model that provided the best fit to our experimental data, datasets were averaged across experiments. Models were fit to all 7 datasets (10 pulses at 50 Hz for control conditions, 100 pulses at 100 Hz for HFS_{100APs}, and 5 times 10 pulses at 50 Hz for test conditions; Figures S4E and S4F), minimizing the sum of squared differences between model and experimental observations. For the second dataset, weight factors were set to 0.2, to compensate for the large number of data points in this set; otherwise, weight factors were set to 1. The total simulation time was set to 122.2 s, to match the experimental time. The model contained 16 free parameters (Table S2). To achieve convergence, we first used a custom-made random search algorithm, in which each starting value was varied by multiplication with a random number drawn from a normal distribution with mean 1 and standard deviation 0.1. Parameter vectors were updated when a reduction of sum of squared differences occurred. For further optimization, FindMinimum of Mathematica was used, which provides an implementation of Brent's principal axis method (https://reference.wolfram.com/language/tutorial/UnconstrainedOptimizationMethodsForLocalMinimization.html#188073100). As datasets before, during, and after PTP were fit simultaneously, the model described PTP in terms of the filling state of the vesicle pools as a function of time.

Statistics and conventions

Statistical significance was assessed using a two-sided Wilcoxon signed rank test for paired comparisons or a two-sided Mann-Whitney U test for unpaired comparisons at the significance level (P) indicated. Multiple comparisons were performed with a Kruskal-Wallis test. Statistical testing was performed with Python 2, MATLAB 2016 or 2018, or Mathematica 12. For electrophysiology data, values and symbols with error bars indicate mean ± standard error of the mean (SEM), unless specified differently. For EM data, values and symbols denote mean ± standard deviation. For graphical representation of statistics, * indicates $p < 0.05$, ** $p < 0.01$, *** $p < 0.001$, and ****, $p < 0.0001$. Membrane potentials are given without correction for liquid junction potentials. In total, data reported in this paper were obtained from 43 GC recordings *in vivo*, 106 mossy fiber terminal–CA3 pyramidal neuron paired recordings *in vitro*, and 581 active zone profiles analyzed by EM.

Supplemental Information

Short-Term Plasticity at Hippocampal Mossy Fiber

Synapses Is Induced by Natural Activity Patterns

and Associated with Vesicle Pool Engram Formation

David Vandael, Carolina Borges-Merjane, Xiaomin Zhang, and Peter Jonas

Figure S1, related to Figure 2. A highly sensitive induction mechanism of hippocampal mossy fiber PTP at near-physiological temperature
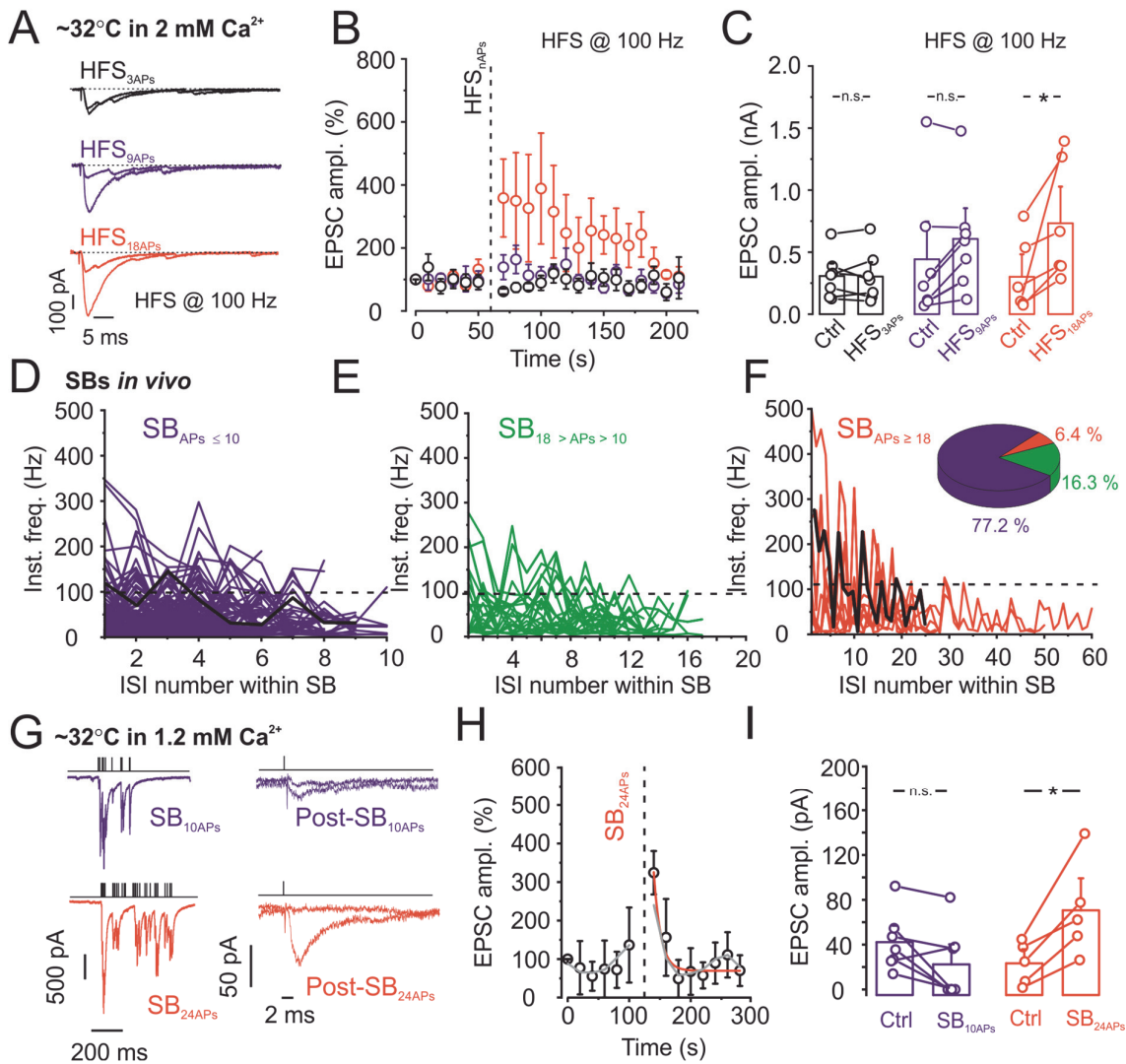
(**A**) Mossy fiber EPSCs under control conditions (black traces) and after HFS$_{3APs}$ (black), HFS$_{9APs}$ (blue), and HFS$_{18APs}$ (red) at near-physiological temperature.

(**B**) Plot of average EPSC peak amplitude against experimental time. HFS$_{3APs}$ (black), HFS$_{9APs}$ (blue), and HFS$_{18APs}$ (red) were applied at the time points indicated by the vertical dashed line.

(**C**) Summary bar graph of PTP at near-physiological temperature. Boxes indicate mean values, error bars denote SEM, and circles show data from individual experiments. In total, data were obtained from 9 mossy fiber terminal–CA3 pyramidal neuron recordings. *, p < 0.05.

(**D–F**) Plot of instantaneous frequency against ISI number for SBs with ≤ 10 APs (D), 11 – 17 APs (E), and ≥ 18 APs (F). Black line in (D) and (E) indicates the SB chosen for subsequent paired recording experiments. Black horizontal dashed line represents 100 Hz frequency used in standard PTP induction protocols.

(**G**) SBs induce PTP at near-physiological temperature and 1.2 mM extracellular Ca^{2+} concentration. Left, EPSCs evoked by SB_{10APs} and SB_{24APs}. Right, EPSCs under control conditions and after PTP induction.

(**H**) Plot of average EPSC peak amplitude against experimental time. SB_{24APs} was applied at the time point indicated by the vertical dashed line.

(**I**) Summary bar graph of PTP at near-physiological temperature and 1.2 mM extracellular Ca^{2+} concentration. As EPSC peak amplitudes in 1.2 mM Ca^{2+} were small, the second EPSC in a 50-Hz train was used for analysis in (H) and (I). Data from 9 pairs. *, $p < 0.05$.

Figure S2, related to Figure 3. Comparison of RRP size estimates for different fitting ranges
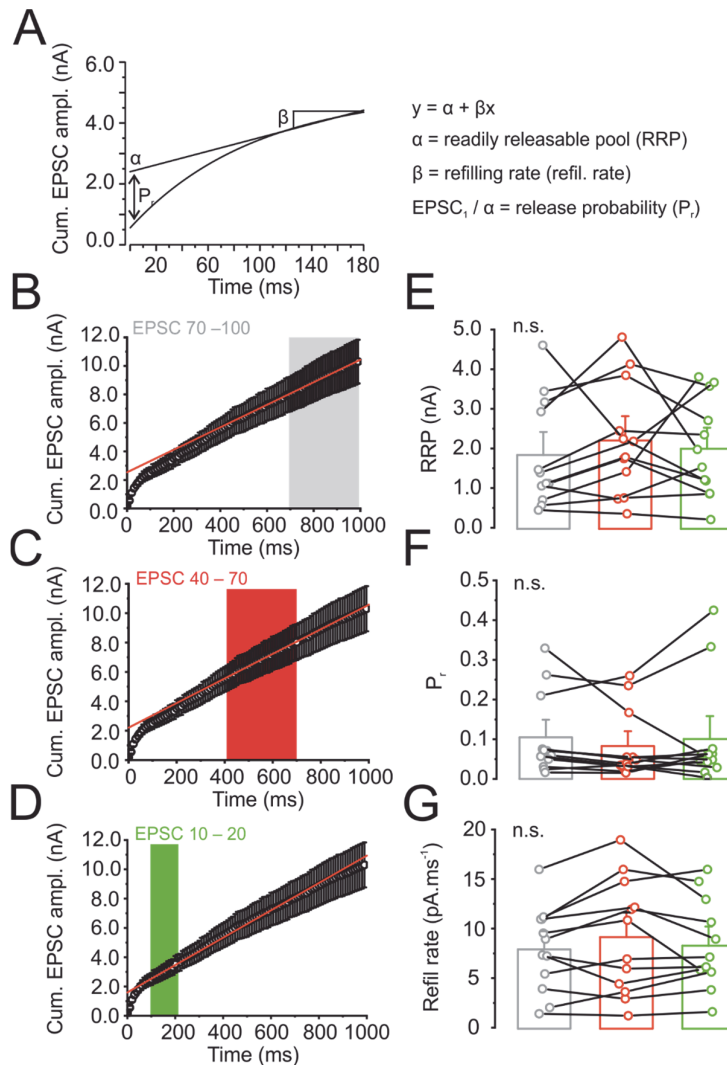

(**A**) Schematic illustration of pool analysis using the SMN method (Schneggenburger et al., 1999; Neher, 2015). Cumulative EPSC peak amplitude during a train stimulation was plotted against time, and data were analyzed by linear regression of the last 3–5 data points. The size of the RRP was determined as the intersection of the regression line with the ordinate, P_r was measured as the ratio of the first EPSC amplitude over RRP size, and refilling rate was obtained from the slope of the regression line.

(**B–D**) Analysis of cumulative EPSC data (100 stimuli, 100 Hz in presynaptic cell-attached stimulation) using the SMN method (Schneggenburger et al., 1999) for different fitting ranges (points 70–100 in (B), gray box; 40–70 in (C), red box; 10–20 in (D), green box).

(**E–G**) Comparison of RRP (E), P_r (F), and refilling rate (G) for the three different fitting ranges. Parameter estimates for the different fitting ranges were similar.

Figure S3, related to Figure 3. Analysis of RRP size in the presence of a low-affinity competitive antagonist reducing AMPA receptor saturation and desensitization
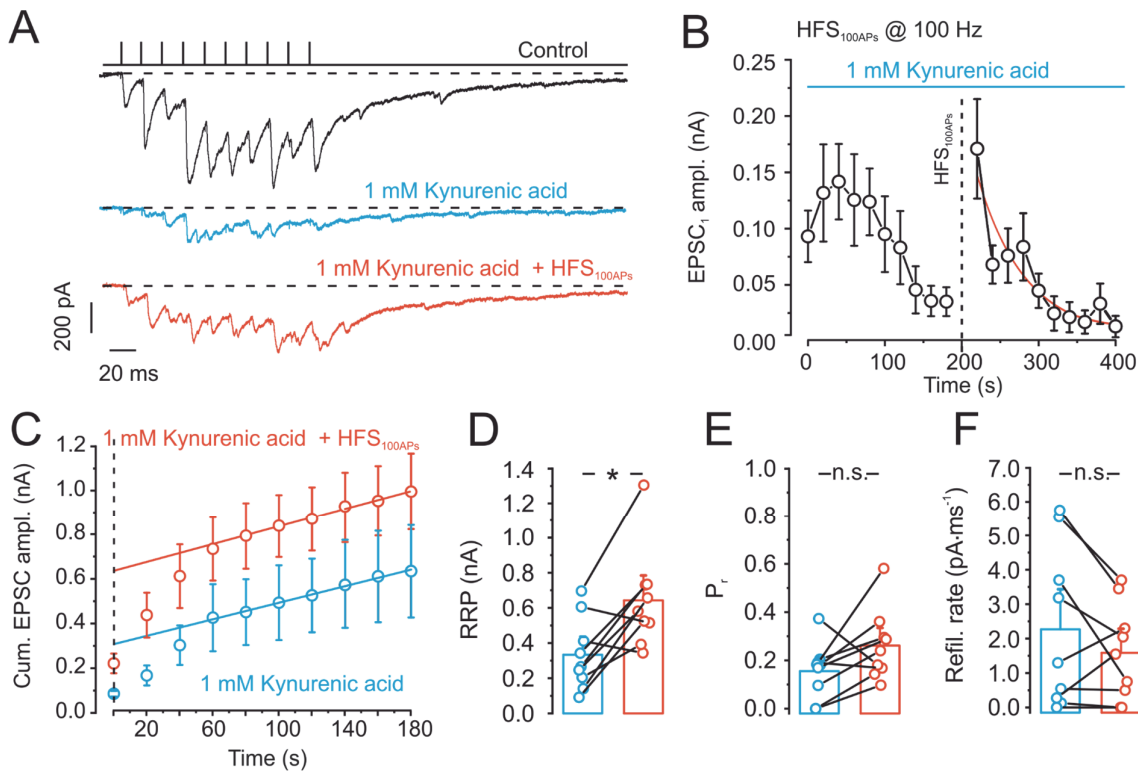

(**A**) Plot of EPSC traces under control conditions (black), in the presence of 1 mM of the low-affinity competitive AMPA receptor antagonist kynurenic acid (light blue), and 20 s after subsequent application of HFS_{100APs} (red).

(**B**) Plot of EPSC peak amplitude against experimental time during application of 1 mM kynurenic acid (horizontal blue continuous line) and subsequent application of HFS_{100APs} (vertical black dashed line). The red curve represents an exponential function fit to the PTP decay phase.

(**C**) Plot of cumulative EPSC peak amplitude during a train stimulation against time. Light blue, control data; red, data 20 s after HFS_{100APs}. Data points during the last 3–5 stimuli (at time points $\geq$ 100–140 ms) were fit by linear regression.

(**D–F**) Summary bar graphs of RRP (D), P_r (E), and refilling rate (F). PTP primarily increased the RRP size, but was associated with much smaller changes in P_r and refilling rate, similar to the results in the absence of the low-affinity competitive AMPA receptor antagonist (**Figures 3**D–3H).

Figure S4, related to Figure 3. Analysis of RRP size using models with time-dependent refilling rate or multiple pools
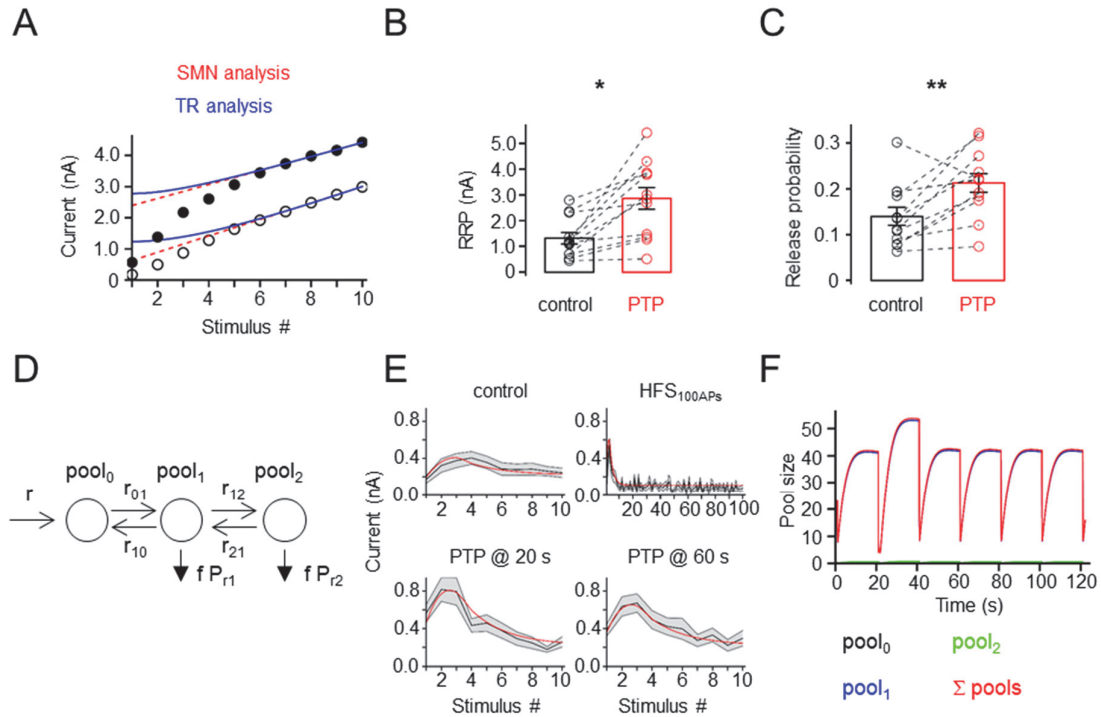
(**A**) Analysis of cumulative EPSC data before and after HFS_{100APs}. Open circles, control data; filled circles, data after HFS_{100APs}. Blue curve indicates fit according to the TR method (Thanawala and Regehr, 2013), assuming that refilling rate increases as release sites are vacated. Red dashed line shows fit according to the SMN method (Schneggenburger et al. 1999), assuming that refilling rate is constant.

(**B** and **C**) Summary bar graphs of RRP size (B) and P_r (C) estimated according to the TR model. Note that the size of the RRP is consistently larger with the TR model than with the SMN model. *, $p < 0.05$; **, $p < 0.01$. Data from 12 pairs.

(**D**) Structure of the three-pool model. The three pools in the model were intended to represent docked, primed, and superprimed vesicle pool (Lee et al., 2013; Taschenberger et al., 2016). f indicates facilitation factor, P_{r1} and P_{r2} indicate different release probabilities of primed and superprimed vesicles, respectively. For additional details, see STAR Methods and Table S2.

(**E**) Analysis of experimental stimulus train responses with the 3-pool model. Top left, control; top right, HFS_{100APs}; bottom left, PTP 20 s after HFS; bottom right, PTP 60 s after HFS. Black line, mean from 12 pairs; gray lines and shaded area, ± SEM range; red line, model prediction.

(**F**) Plot of size of the three pools as a function of time. Black, $pool_0$; blue, $pool_1$; green, $pool_2$; red, sum of all pools. Test stimulations (10 APs at 50 Hz) were applied every 20 s; HFS_{100APs} was simulated at 20 s (dashed vertical line). Note that $pool_2$ was only minimally populated, suggesting a low abundance of "superprimed" vesicles (Lee et al., 2013; Taschenberger et al., 2016) at hippocampal mossy fiber synapses in our experimental conditions.

5

Figure S5, related to Figure 3. Dependence of PTP on extracellular Ca²⁺ concentration
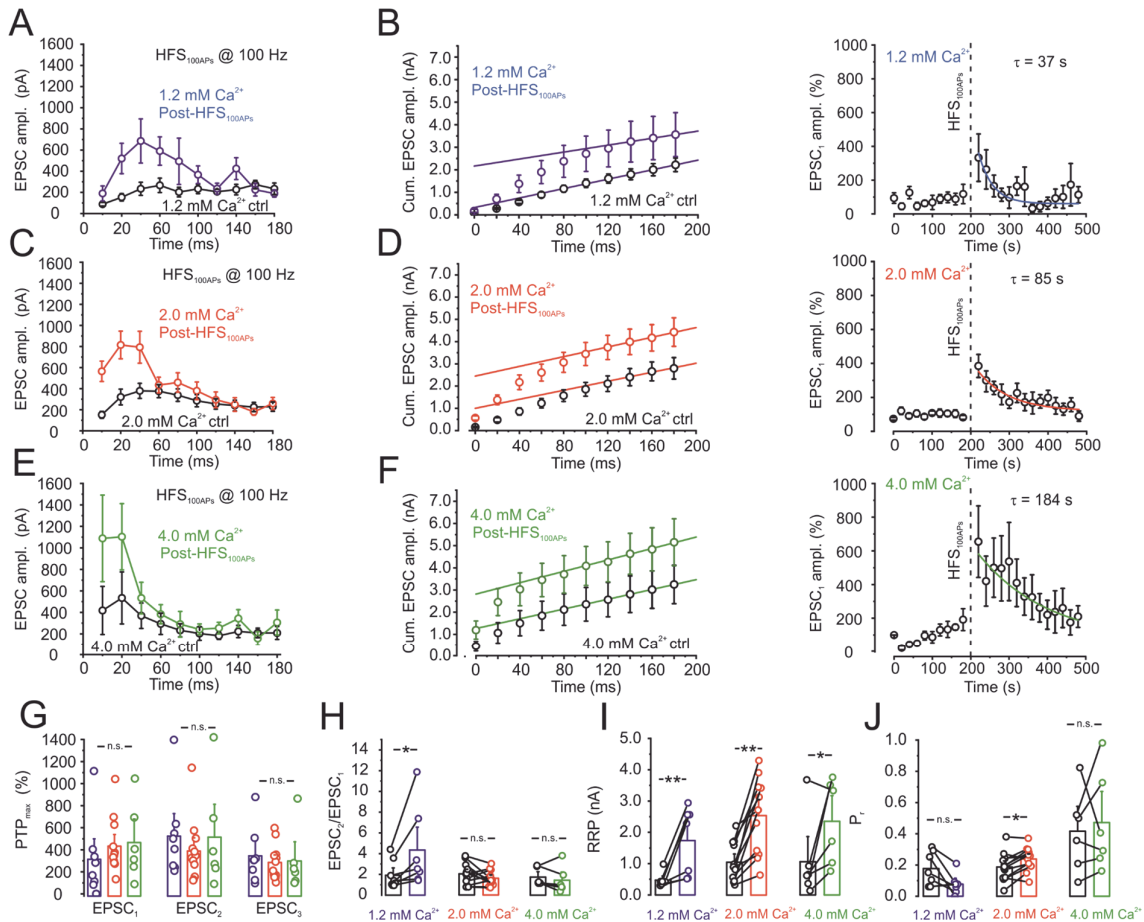
(**A** and **B**) Plot of EPSC amplitude during 50-Hz test trains of 10 stimuli under control conditions (black) and after HFS$_{100APs}$ (purple) in 1.2 mM extracellular Ca²⁺ (A), plot of cumulative EPSC peak amplitude (B, left), and plot of average EPSC peak amplitude against experimental time for first EPSC (B, right). HFS$_{100APs}$ was applied at the time point indicated by the vertical dashed line. Curve in (B, right) indicates exponential function fit to the PTP decay phase.

(**C–F**) Similar plot as in (A and B), but for 2 mM Ca²⁺ (C and D) and 4 mM Ca²⁺ (E and F).

(**G**) Summary bar graph of PTP for 1.2, 2, and 4 mM extracellular Ca²⁺.

(**H**) Summary of paired-pulse ratio (EPSC$_2$ / EPSC$_1$) in 1.2, 2, and 4 mM Ca²⁺. Note that paired-pulse ratio paradoxically increases after PTP induction in 1.2 mM Ca²⁺.

(**I** and **J**) Summary bar graph of changes in RRP (I) and P$_r$ (J) after PTP.

In total, data were obtained from 9 mossy fiber terminal–CA3 pyramidal neuron recordings. *, $p < 0.05$; **, $p < 0.01$.

6

Figure S6, related to Figure 5. Functional EM reveals pool overfilling after PTP induction
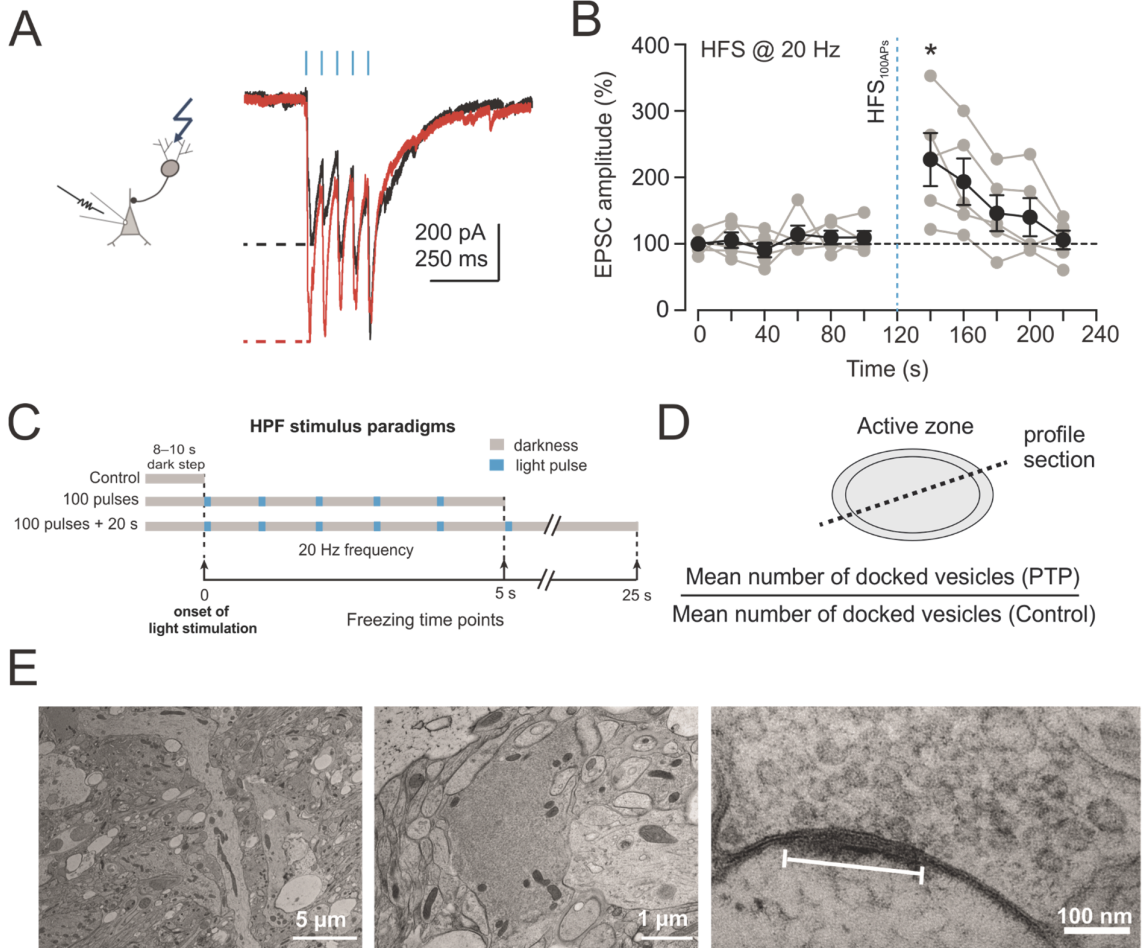
(**A**) Optogenetically evoked EPSCs in CA3 pyramidal neurons. Black, control; red, trace after HFS$_{100APs}$. Blue lines indicate light pulses.

(**B**) Plot of EPSC peak amplitude against time before and after HFS$_{100APs}$. Gray, individual experiments; black, average from 5 recordings. Blue vertical dashed line indicates HFS$_{100APs}$. Recordings were performed at near-physiological temperature (Borges-Merjane et al., 2020). *, $p < 0.05$.

(**C**) Schematic illustration of stimulation–freezing paradigms used in the present set of experiments.

(**D**) Schematic illustration of analysis of number of docked vesicles per profile. Note that the number of vesicles per active zone (a 2-dimensional structure) is expected to be quadratically related to the number of vesicles per profile (a 1-dimensional structure).

(**E**) Electron micrographs of hippocampal mossy fiber synapses at different magnification. White bar in right micrograph indicates postsynaptic density.

Figure S7, related to Figure 7 and Discussion. Unique mechanisms of PTP enable flexible synaptic computations.
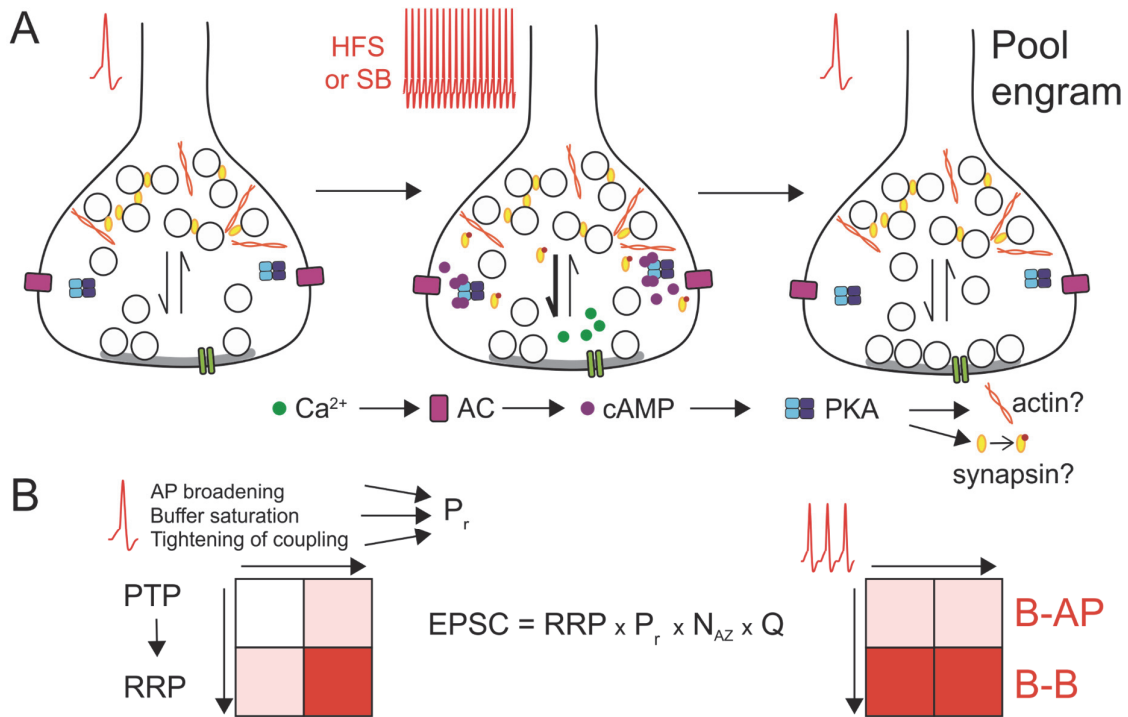
(**A**) Mechanisms of PTP induction. Sensitivity of PTP to PKA blockers and actin polymerization inhibitors suggest that HFS enhances refilling of readily releasable and docked vesicle pools. A possible molecular link between PKA and actin is represented by synapsin (Gitler et al., 2008).

(**B**) Orthogonal forms of presynaptic plasticity at hippocampal mossy fiber synapses enable flexible synaptic computations. Left, AP broadening, buffer saturation, and tightening in source-sensor coupling are known to change release probability during facilitation or long-term potentiation (Geiger and Jonas, 2000; Vyleta and Jonas, 2014; Midorikawa and Sakaba, 2017). In contrast, PTP primarily increases pool size. As the EPSC peak amplitude is the product of RRP, release probability (P_r), number of active zones (N_{AZ}), and quantal size (Q), changes in RRP and P_r may affect synaptic efficacy multiplicatively (as indicated by color intensity). Right, changes in RRP and P_r could differentially regulate mossy fiber detonation (Henze et al., 2002; Vyleta et al., 2016). Increase in RRP promotes a burst-to-burst transmission mode, whereas increase in P_r shifts the synapse towards a burst-to-spike transmission regime.

Table S1, related to Figure 2. Basic properties of unitary EPSCs at hippocampal mossy fiber–CA3 pyramidal neuron synapses

Parameter	Value before PTP (mean ± SEM, n pairs)	Value after PTP (20 s)
Synaptic delay (ms)	1.47 ± 0.08 (n = 12)	1.45 ± 0.15 (n = 12)
20–80% EPSC rise time (ms)	0.9 ± 0.07 (n = 12)	1.1 ± 0.09 (n =12)
EPSC peak amplitude (pA)	180.8 ± 55.16 (n = 12)	564.5 ± 97.05 (n = 12)
EPSC decay time constant (ms)	6.9 ± 0.42 (n = 12)	5.6 ± 0.28 (n = 12)
PTP (%) Induction by HFS_{100APs}	432 ± 74 (n = 12)	
Mossy fiber mEPSC peak amplitude (median)	41.8 ± 3.3 (n = 8)	45.7 ± 3.6 (n = 8)
Mossy fiber mEPSC peak amplitude (mean)	52.9 ± 3.2 (n = 8)	59.9 ± 4.2 (n = 8)
Total mEPSC peak amplitude (median)	29.9 ± 1.5 (n = 13)	

Evoked EPSC experiments were performed with presynaptic tight-seal cell-attached stimulation.

Miniature EPSC (mEPSC) experiments were performed in the presynaptic whole-cell configuration. Mossy fiber mEPSCs were recorded during presynaptic depolarization. Total miniature mEPSCs (including both mossy fiber and non-mossy fiber contributions) were collected during the entire recording time.

Values indicate mean ± SEM. PTP was induced by HFS_{100APs}.

Table S2, related to Figure 3. Vesicle pool model describing EPSC train responses

Parameter	Optimal value
N	23.1
r_{01}	85.5 ms^{-1}
r_{10}	0.010 ms^{-1}
r_{12}	0.052 ms^{-1}
r_{21}	3.929 ms^{-1}
P_{r1}	0.173
P_{r2}	0.202
r_0	0.178 ms^{-1}
r_1	0.014 ms^{-1}
τ_r	918.3 ms
K_r	2.398
m_r	0.329
f_{max}	2.374
K_f	0.916
m_f	7.012
r_{spont}	2.824 10^{-6} ms^{-1}

Models were fit to all 7 data sets (10 pulses at 50 Hz for control conditions, 100 pulses at 100 Hz for HFS$_{100APs}$, and 5 times 10 pulses at 50 Hz for test conditions). Starting values were determined by a custom-made random search algorithm, and optimization was performed using a Brent's principal axis method. Parameter range was set to [0, 1000] for pool size N, [0–0.01, 100] for rates r, [0.0001, 1] for release probabilities P_r, [2, 1000] for facilitation factor f_{max}, [0.5, 100] for affinities K, [0.01, 10] for exponents m, and [0, 0.01] for spontaneous release rate r_{spont}. For details, see STAR Methods.